

The Pore-Lipid Interface: Role of Amino-Acid Determinants of Lipophilic Access by Ivabradine to the hERG1 Pore Domain[§]

Laura Perissinotti,¹ Jiqing Guo,¹ Meruyert Kudaibergenova,¹ James Lees-Miller, Marina Ol'khovich, Angelica Sharapova, German L. Perlovich, Daniel A. Muruve, Brenda Gerull, Sergei Yu Noskov, and Henry J. Duff

Centre for Molecular Simulation, Department of Biological Sciences, University of Calgary, Calgary, Alberta, Canada (L.P., M.K., S.Y.N.); Libin Cardiovascular Institute of Alberta (J.G., J.-L.M., H.J.D.) and Snyder Institute for Chronic Diseases (D.A.M.), Cumming School of Medicine, University of Calgary, Calgary, Alberta, Canada; Institute of Solution Chemistry, Russian Academy of Sciences, Ivanovo, Russian Federation (M.O., A.S., G.L.P.); Department of Cardiac Sciences and Libin Cardiovascular Institute of Alberta, University of Calgary, Calgary, Alberta, Canada (B.G.); and Comprehensive Heart Failure Center and Department of Internal Medicine I, University Hospital Würzburg, Würzburg, Germany (B.G.)

Received December 21, 2018; accepted May 28, 2019

ABSTRACT

Abnormal cardiac electrical activity is a common side effect caused by unintended block of the promiscuous drug target human *ether-à-go-go*-related gene (hERG1), the pore-forming domain of the delayed rectifier K⁺ channel in the heart. hERG1 block leads to a prolongation of the QT interval, a phase of the cardiac cycle that underlies myocyte repolarization detectable on the electrocardiogram. Even newly released drugs such as heart-rate lowering agent ivabradine block the rapid delayed rectifier current I_{Kr}, prolong action potential duration, and induce potentially lethal arrhythmia known as torsades de pointes. In this study, we describe a critical drug-binding pocket located at the lateral pore surface facing the cellular membrane. Mutations of the conserved M651 residue alter ivabradine-induced block but not by the common hERG1 blocker dofetilide. As revealed by molecular dynamics simulations, binding of ivabradine to a lipophilic pore access site is coupled to a state-dependent reorientation of aromatic

residues F557 and F656 in the S5 and S6 helices. We show that the M651 mutation impedes state-dependent dynamics of F557 and F656 aromatic cassettes at the protein-lipid interface, which has a potential to disrupt drug-induced block of the channel. This fundamentally new mechanism coupling the channel dynamics and small-molecule access from the membrane into the hERG1 intracavitary site provides a simple rationale for the well established state-dependence of drug blockade.

SIGNIFICANCE STATEMENT

The drug interference with the function of the cardiac hERG channels represents one of the major sources of drug-induced heart disturbances. We found a novel and a critical drug-binding pocket adjacent to a lipid-facing surface of the hERG1 channel, which furthers our molecular understanding of drug-induced QT syndrome.

Introduction

The cardiac action potential is primarily generated by sodium and calcium channels, which depolarize the membrane potential, and by potassium channels, which repolarize

the membrane potential and terminate the action potential (Nerbonne and Kass, 2005). Gene mutations, age-related factors, and drug-induced toxicity are all linked to various perturbation of action potentials, leading to potential lethal disorders of heart rhythm (arrhythmias) (Chiamvimonvat et al., 2017). Several K⁺-selective channels were identified as major determinants of proarrhythmic activity and main targets in antiarrhythmic drug development. Perhaps the most impactful of these is the human *ether-a-go-go*-related gene 1 (hERG1 or Kv11.1) channel, the K⁺-selective channel carrying the rapid delayed rectifier current (I_{Kr}) in myocytes (Trudeau et al., 1995). The physiologic role of I_{Kr} is to repolarize the late phase of cardiac action potential; hence, currents carried by hERG1 that contain human mutations are linked to arrhythmias (Gustina and Trudeau, 2009; Vandenberg et al., 2012). Likewise, pharmacological blockage of the I_{Kr} can lead to

This work was supported by the Canadian Institutes of Health Research Project Grant FRN-CIHR: 156236 (to J.G., J.L.-M., and H.J.D.); the National Institutes of Health [Grant R01HL128537-01 (S.Y.N., J.G., L.P., and M.K.)]; and the Discovery grant from the Natural Scientific and Engineering Research Council of Canada (to H.J.D.). Computational support for this work was partially provided by West-Grid Canada through a resource allocation award to S.Y.N. M.K. was supported by a Queen Elizabeth II graduate scholarship. Anton 2 computer time was provided by the Pittsburgh Supercomputing Center (PSC) through Grant R01GM116961 from the National Institutes of Health. The Anton 2 machine at PSC was generously made available by D.E. Shaw Research.

¹L.P., J.G., and M.K. contributed equally to this work.

<https://doi.org/10.1124/mol.118.115642>.

[§] This article has supplemental material available at molpharm.aspetjournals.org.

ABBREVIATIONS: cryo-EM, cryoelectron microscopy; hERG1, human *ether-à-go-go* 1 gene in reference to α -subunit of Kv10.1 K⁺ channel; hERG1, the human *ether-à-go-go*-related gene in reference to α -subunit of Kv11.1 K⁺ channel; IFD, Induced-Fit Docking; I_{hERG1}, current carried by hERG1; I_{Kr}, rapid delayed rectifier current; MD, molecular dynamics; WT, wild-type.

a prolongation of the QT interval (phase 3 repolarization), causing a drug-induced long-QT syndrome (Compton et al., 1996; Roden et al., 1996; Splawski et al., 1997; Huang et al., 2001; Vandenberg et al., 2001). Drug-induced block of hERG1 and its associated prolongation of the QT interval and proarrhythmia has resulted in hERG1 being one of the most studied ion channels (Numaguchi et al., 2000; Witchel, 2011; Sanguinetti, 2014). Recent high-throughput screening studies have provided additional evidence for the central role of hERG1 blockade in drug-safety assessments (Di Veroli et al., 2013a).

Despite the plethora of experimental data available for drug interactions with the hERG1 channel, a-priori prediction of the cardiotoxic potential of a novel compound during a preclinical developmental stage is a complex and a challenging task. The torsadogenicity is an emergent and a complicated property that depends on several factors: the conformational state of the channel being targeted by the compound (Chen et al., 2002; Stork et al., 2007; Lees-Miller et al., 2015; Wu et al., 2015), general kinetics of the drug access mechanisms (Guo et al., 2005; Di Veroli et al., 2013b; Hill et al., 2014), the solubility of the drug in the membrane (Wacker and Noskov, 2018), patient-to-patient variance in isoform composition of hERG1 (hERG1a/hERG1b) (Sale et al., 2008), and isoform-specific interactions with blockers (Abi-Gerges et al., 2011). Given these factors, understanding molecular determinants of drug-induced QT-prolongation remains one of the fundamental and elusive problems in the field of molecular pharmacology. Even newly released “cardio-safe” drugs entering the market, such as ivabradine, are found to block the I_{Kr} , prolong action potential duration, and can contribute to a potentially lethal drug-induced arrhythmia known as torsades de pointes (Duff et al., 1995; Lees-Miller et al., 2000, 2015; Chen et al., 2002; Melgari et al., 2015).

Ivabradine is commonly prescribed as a blocker of I_f (funny current) and acts as a heart-rate lowering agent for symptomatic management of the chronic heart failure. However, over a similar range of concentrations, the drug also blocks hERG; thus, ivabradine prolongs phase 3 of the action potential and has been reported to induce torsades de pointes when applied in a poly-pharmaceutical context (Hancox et al., 2015; Melgari et al., 2015; Frommeyer et al., 2017). In a previous study, by combining electrophysiology and molecular modeling techniques, we emphasized the importance of the lipophilic interface and high-affinity state-dependent blockade of hERG1 by ivabradine (Lees-Miller et al., 2015). The molecular simulations performed on the homology model of hERG1 pore domain in open and closed states indicated that ivabradine may bind to a lipid-facing binding pocket centered at the M651 residue (Lees-Miller et al., 2015). However at the time, findings were limited owing to the lack of structural information on the organization of the pore domain of the hERG1 channel. In 2017, a high-resolution cryoelectron microscopy (cryo-EM) structure (3.4 Å) of a highly homologous neuronal human ether à go-go 1 gene (hEAG1) channel was resolved with a voltage-sensor in a depolarized (open) state, but with the pore domain closed. Later in the same year, the high-resolution structure of the hERG1 channel (3.2 Å) was reported in the open state (Whicher and MacKinnon, 2016; Wang and MacKinnon, 2017) (Fig. 1). These new structural atomic details provided the opportunity to unravel the potential lipophilic access mechanisms for the ivabradine-induced block of hERG1, to assess the impact of mutations at the M651 site in the distal S6, and to

understand the dynamics of allosteric coupling between residues involved in the high-affinity channel block.

Herein, we report an in-depth study that provides direct evidence of ivabradine's interaction in a state-dependent manner with lipid-facing residues as part of the hERG1 blockade process. We assessed whether mutations of the lipid-facing residues, when coupled with C-type inactivation impacting mutations, affect the concentration of ivabradine required to block the hERG1 current. To reveal mechanisms involved in coupling dynamics of the lipid-facing residues with respect to the aromatic cassette involved in high-affinity drug block by various compounds (Fig. 1), we performed several multi-microsecond molecular dynamics (MD) simulations of the wild-type (WT) and mutated forms of hERG1 in conjunction with molecular biology and electrophysiological studies. The MD simulations in combination with the ensemble docking simulations allowed us to map molecular details of the probable lipophilic access pathway of ivabradine and potentially explain the drug's dependence on the inactivation process of hERG1 channel. Our results show that ivabradine's binding at the vicinity of the lipid-facing residue M651 is directly coupled to the conformational dynamics (reorientation) of the aromatic cassettes (F656 and F557) in the S6 (Fig. 1, A and B). Disruption of this allosteric coupling between drug binding on the lipid-facing surface and conformational dynamics of F656/F557 was shown to greatly attenuate ivabradine blockade.

Materials and Methods

Molecular Biology. Methods for site-directed mutagenesis have been previously reported (Lees-Miller et al., 2015; Wang et al., 2016). The hERG1 constructs were transfected into mammalian human embryonic kidney cells. Single- and double-mutant constructs of hERG1 were produced using conventional overlap polymerase chain reaction with primers synthesized by Sigma Genosys (Oakville, ON, Canada) and sequenced using Eurofins MWG Operon (Huntsville, AL). Constructs were linearized with XbaI restriction endonuclease, and cRNA was transcribed in vitro using the mMessage mMachine T7 Ultra cRNA transcription kit (Ambion, Austin, TX).

General Setup for Electrophysiological Recordings. The extracellular solution contained (in millimolars) NaCl 140, KCl 5.4, CaCl_2 1, MgCl_2 1, HEPES 5, and glucose 5.5; the pH of the solution was adjusted and kept at 7.4 with NaOH. Micropipettes were pulled from borosilicate glass capillary tubes on a programmable horizontal puller (Sutter Instruments, Novato, CA). The pipette solution contained the following: 10 mM KCl, 110 mM K-aspartate, 5 mM MgCl_2 , 5 mM Na_2ATP , 10 mM EGTA (ethylene glycol-bis-(aminoethyl ether)- N,N,N,N tetraacetic acid), 5 mM HEPES, and 1 mM CaCl_2 ; the solution was adjusted to pH 7.2 with KOH. Standard patch-clamp methods were used to measure the whole-cell currents of hERG1 mutants expressed in human embryonic kidney 293 cells using the AXOPATCH 200B amplifier (Axon Instruments). Unless otherwise indicated, the tail currents were recorded when the voltage was returned to -100 mV from $+50$ mV. Transfected human embryonic kidney cells were patched to record the hERG1 currents. Ivabradine was directly dissolved into the Tyrode solution right before the experiments. The solutions were used for the next 2 hours during the experiments. The stock solution of $100 \mu\text{M}$ ivabradine was prepared in the extracellular solution. Fresh stock solutions of ivabradine were prepared weekly.

Voltage-Dependence of Activation. From a holding potential of -80 mV cells were depolarized for 1 second to a range of voltages from -100 to $+40$ mV followed by a step to -100 mV (1 second) to

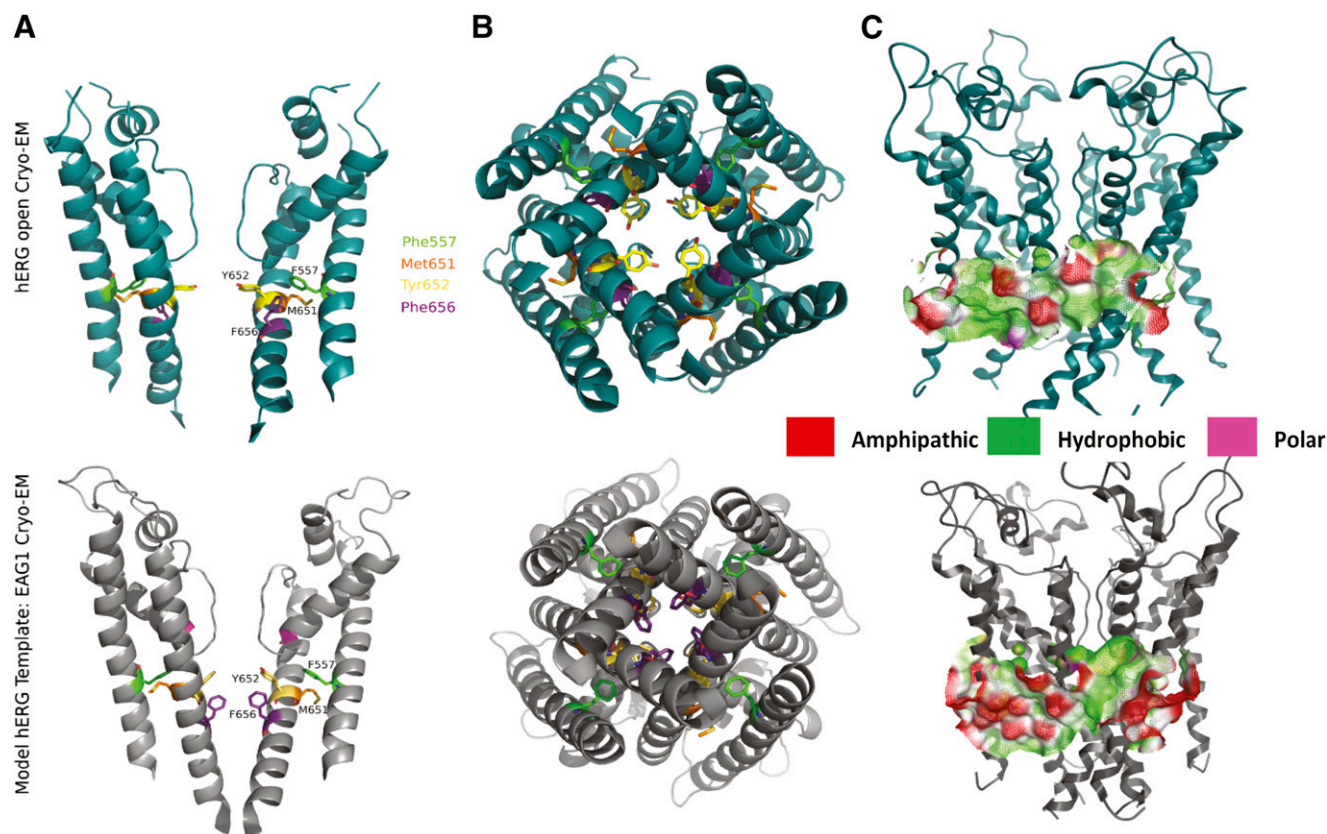


Fig. 1. Structural organization of drug binding site in the intracellular cavity of hERG1 channel. (A) Organization of the hERG1 pore domain (two subunits are shown for clarity) in the open (top) and closed (bottom) states, respectively. The location of key residues involved in the state-dependent dynamics of membrane-facing side windows is shown in color-coded stick mode. (B) Access pathway to the intracellular cavity of hERG1 channel from the intracellular milieu. The differences in orientation of key hydrophobic residues involved to ivabradine-induced block are shown for the open (top) and closed (bottom) states, respectively. (C) The trajectory-averaged iso-surfaces available for the drug's lipophilic access to the intracellular cavity. The residue-based color coding was used to highlight protein-membrane interfaces present in the open (top) and closed (bottom) states of the channel, respectively.

record the tail currents. The isochronal tail-current-voltage plots were fit to a single Boltzmann function (1):

$$\frac{I}{I_{max}} = \frac{1}{1 + \exp\left[\frac{(V_{1/2} - V_m)}{k}\right]} \quad (1)$$

where I/I_{max} is the normalized current, $V_{1/2}$ is voltage of the half-maximal activation, k is the slope factor, and V_m is the membrane potential.

Analysis of Deactivation. Deactivation of hERG1 tail currents was measured by activating channels at +40 mV, followed with a short (5-millisecond) repolarization step to -120 mV and deactivating steps at -120, -100, -60, and -40 mV. Currents at different voltages were normalized and fitted. The fitted data were averaged ($n = 10$).

Statistical Analysis of Electrophysiological Experiments. Statsview (Abacus Concepts, Berkeley, CA) or QTI plot (Vasilef, 2013), Grace (<http://plasma-gate.weizmann.ac.il/Grace/>) were used to analyze the data. The null hypothesis of this study predicted no difference between the IC_{50} values of the single mutation to the double mutations assessed. The null hypothesis was rejected when the P value was <0.05 as evaluated by a one-way analysis of variance with Tukey test. The exact P values for data in Fig. 4 are presented in the Supplemental Table 1. All variance measures (bars) for electrophysiological data are shown as S.D. The study was exploratory, thus there was no a priori reason to consider whether there was an additive or subtractive interaction. In addition, we acknowledge that there may be other mutations, unknown to us at this time, which could be relevant. All of the comparisons were prespecified and all of the comparisons are reported. A priori, we generally required a minimum

of $n = 2$ independent experiments for each point on the IC_{50} curve. However, the n values near the IC_{50} point and near the maximum blockade have a major impact on the reliability of the IC_{50} estimate. Frequently we increased the n values at these putative points to be more certain about the reliability of the measurement. The n values for each point of the concentration-response relationship are presented in the figure legends. J.G. executed the experiments and analyzed the experimental data, hence he was not blinded. However, each experiment was reviewed by a small committee of individuals to assess quality of the records at weekly laboratory meetings (J.G. and H.J.D.) and on a monthly basis (H.J.D. and S.Y.N.) to review raw experimental data.

Dofetilide and Ivabradine Water/Hexane Partitioning Experiments. The distribution coefficient for dofetilide and ivabradine were determined by the use of a classic shake-flask method detailed in our previous publications (Perlovichl and Bauer-Brandl, 2003; Perlovich et al., 2006; Blokhina et al., 2016). Prior to conducting the experiments, both solvents were mutually saturated to reach equilibrium by slow stirring into a biphasic system for 2 days. Ivabradine and dofetilide were dissolved in a buffer at pH=7.4 and then were added to a hexane solution. To ensure complete equilibration of the system as indicated by the absence of turbidity on each phase, the flasks were shaken for about 48 hours in a thermostatic water bath at 293.15, 298.15, 303.15, 310.15, and 313.15 K. After reaching equilibration in the system, the samples from the lower phase were carefully removed with syringes for analysis. The molar concentrations of the dofetilide and ivabradine in the buffer phase were measured by a Cary-50 spectrophotometer (Varian) with an accuracy of 2%–4%. The experimental results are reported as an average value of at least three

replicated experiments. The accuracy of the distribution coefficients were verified by comparing the starting mass of a compound and the total mass of the compound distributed in the two phases. The reproducibility of the measured concentrations was under 0.1%, and the maximum deviations from the average value were <0.15%. The ratio of the compound equilibrium concentration in mole fraction in the hexane phase (x_H) to those in the aqueous phase (x_B) was determined using the hexane/buffer distribution coefficient in the following form:

$$D_{H/B} = x_H/x_B \quad (2)$$

$D_{H/B}$ is the phase equilibrium constant for a drug distributed in the hexane phase and the saturated buffer phase.

The standard Gibbs energy of transfer $\Delta_{tr}G^\circ$ from the buffer into an organic solvent was calculated by using:

$$\Delta_{tr}G^\circ = -RTD_{H/B} \quad (3)$$

The temperature dependence of distribution (van't Hoff method) was employed to obtain the enthalpy of transfer $\Delta_{tr}H^\circ$:

$$\frac{d(\ln D^*)}{dT} = \frac{\Delta_{tr}H^\circ}{RT^2} \quad (4)$$

The entropy of transfer $\Delta_{tr}S^\circ$ was calculated from:

$$\Delta_{tr}S^\circ = (\Delta_{tr}H^\circ - \Delta_{tr}G^\circ)/T \quad (5)$$

In-depth details on the partitioning experiments and quality controls are provided in the Supplemental Materials.

Molecular Dynamics Simulations. The three-dimensional structure for the open state of the channel in this study is the recently published high-resolution cryo-EM structure of the transmembrane domain of hERG1 channel (PDB ID 5VA2). The structure was truncated before the Per-Arnt-Sim domain (PAS) and after cyclic nucleotide-binding domain domains as described in our previous publication (Wacker et al., 2017; Perissinotti et al., 2018). The basis for the three-dimensional structure for the closed-state hERG1 channel is the homology modeling of hEAG1 with template derived from the cryo-EM structure (PDB ID 5K7L) solved at 3.78 Å resolution. The SWISS-MODEL program (Kopp and Schwede, 2004) was used to develop the hERG1 closed homology model from the available hEAG1 channel structure. Sequence alignment was performed using the CLUSTALW algorithm (Thompson et al., 1994). The sequence similarity between hERG1 and hEAG1 channels for the pore domain (S5–S6) is over 75% (Wacker et al., 2017). The detailed analysis of two structures was published recently (Vandenberg et al., 2017; Wacker et al., 2017). The main differences between pore domains of the two channels are located in the extended turret region connecting S5 to the pore helix. The following three-step protocol was adapted to model missing residues and flexible elements: 1) threading for generation of initial models on the basis of template structure by copying coordinates over the aligned regions (for closed states), 2) low-resolution ROSETTA loop modeling using the cyclic coordinate descent method, 3) high-resolution all-atom refinement and selection of models on the basis of ROSETTA clustering (Bender et al., 2016).

Models of the protein were generated from the alignment in a stepwise manner. CHARMM-GUI (Jo et al., 2008) was used to prepare protein–dipalmitoylphosphatidyl choline lipid bilayer complexes solvated in 150 mM KCl aqueous solution using CHARMM-36 force-field and TIP3P water model (Jorgensen et al., 1983; MacKerell et al., 1998; Noskov et al., 2004; Noskov and Roux, 2008; Klauda et al., 2010; Best et al., 2012). The fully assembled systems were equilibrated for 10 nanoseconds using NAMD2.10 (Phillips et al., 2005) and then subjected to production runs with the Anton 2 supercomputer. The production runs were performed for 1.0–2.5 microseconds, each with CHARMM36M (Huang et al., 2017) force-field to assess structural dynamics of residues involved in lipophilic access in hERG1 WT and

selected mutants. The production runs were executing in a semi-isotropic (NPA-T) ensemble at a temperature of 315 K maintained by the Nosé-Hoover thermostat (Martyna et al., 1994). The time-step for production runs was set to 2 femtoseconds, and trajectories were saved every 240 picoseconds. Nonbonded and long-range electrostatic interactions were evaluated every 2 and 6 femtoseconds, respectively. Long-range electrostatics was calculated using the k-Gaussian–Ewald method implemented to enhance performance on Anton 2 platform (Shan et al., 2005; Shaw et al., 2014) with a 64 Å × 64 Å × 64 Å grid. SHAKE was used to constrain all bonds involving hydrogen atoms. All of the subsequent trajectory analysis was performed using the CHARMM c40b2 program package (Brooks et al., 2009).

Molecular Docking Protocols. Ivabradine in neutral and charged states was docked in-silico to the hERG1 open- and closed-pore structures to establish binding modes. This was performed via the Induced-Fit Docking (IFD) approach available in the Schrödinger Suite (Schrödinger LLC, 2016). Schrödinger's IFD protocol uses Glide and Prime to exhaustively consider possible binding modes and the associated conformational changes within the receptor's active sites (Schrödinger LLC, 2016). In addition to the well established high-affinity binding pocket in the intracellular cavity of hERG1 channels, previous blinded docking studies revealed several alternative binding regions present in the hERG1 homology models and the cryo-EM-derived structures (Lees-Miller et al., 2015; Saxena et al., 2016; Wacker et al., 2017). To map these alternative binding pockets as accurately as possible, we adapted the following two-step protocol. First, a blind docking was performed covering an entire receptor (e.g., pore and voltage-sensing domains regions of hERG1), and then elucidated common binding sites were selected for further studies with high-precision grid mapping. The SiteMap module of the Schrödinger molecular modeling package was used to generate fine-grids for the subsequent precision docking. Following previously tested protocols, the grid was defined to 15 “site-points” for each pocket found during the blinded docking run (Schrödinger LLC, 2016). Then, site maps are cropped 10 Å from the nearest site-point (Halgren, 2009). The scoring was carried out using Schrödinger's discretized version of the ChemScore empirical scoring function, resulting in a small number of best-refined poses, following which the best-docked protein-ligand complex was determined on the basis of a model energy score (E_{model}) that combined the energy of the grid-score, the binding affinity predicted by GlideScore, and (for flexible docking) the internal strain energy for the model potential used to direct the conformational-search algorithm (Schrödinger LLC, 2016). The basis for the partial charges for the neutral form of the drug was the nonbonded parameters from the Optimized Potentials for Liquid Simulation Force Field (OPLS3) with parameters specifically optimized for drug-like molecules (Harder et al., 2016). For all docking simulations the funnel width was increased by adjusting the energy window to 5.0, the CvdW cutoff was set to 10.0 kcal/mol, and the clustering criteria was set to 0.75 and extra-precision (XP) (Friesner et al., 2006). In addition to the single-structure docking procedure, MD-generated ensembles for the open hERG1 transmembrane and mutant forms were used in an ensemble docking with ivabradine to account for the conformational dynamics of the pore domain. A similar protocol was used in a comparative study of a cationic ivabradine binding to the main intracavitary site present in the open state of hERG1.

Ensemble Docking Procedure. From the last 1.0 microseconds of the production MD trajectories, we randomly selected 25 frames spaced every 40 nanoseconds. The basis of the alignment of each frame was the position of the backbone atoms from the pore domain (residues 545–572 and 635–669). Glide was used with the XP ensemble docking (Friesner et al., 2006) with Schrödinger Small-Molecule Drug Discovery Suite 2018-2 (2016) as described above for the single-structure docking protocol. The ligand binding site defined in a single-structure receptor docking was the basis for the generation of each receptor grid. Each generated grid is made of two boxes: the inner box for searching docking space that defines acceptable volume for the ligand center to

explore and the outer box for searching the space of valid poses that must contain all ligand atoms for which grid potentials are computed. The inner cubic box was fixed at the dimension of $15 \text{ \AA} \times 15 \text{ \AA} \times 15 \text{ \AA}$ and the outer box was set to $30 \text{ \AA} \times 30 \text{ \AA} \times 30 \text{ \AA}$. The number of selected docking poses per docking simulation was set to approx. 50, and only poses with binding affinities of $< -3 \text{ kcal/mol}$ were clustered. It is important to mention that grids generated by the SiteMap protocol were overlapping. Therefore, poses obtained from separate docking simulations were clustered into three sites on the basis of where the ligand was bound.

The first site corresponds to all poses found inside the intracellular cavity of the receptor (within approx. 3 \AA of the C_α atoms of Y652 or F656); poses on the lipid-facing transmembrane domain (lipophilic, within approx. 3 \AA of the C_α atom of M651) maps lipophilic site 2 and poses found between transmembrane segments of the pore domain (S5–S6) and the voltage sensing domain (S1–S4) map a putative “access path” site 3.

Results

Rationale for the Selection of Mutants. Our previous in-silico screening of ivabradine binding to the hERG1 model representing open and closed states of the channel identified several potential binding modes (Lees-Miller et al., 2015). The best-scored binding poses for neutral and cationic ivabradine were clustered around a well known intracavitary site in the open state of hERG1; however, almost no binding in the internal cavity (Y652-F656) was observed for the closed-state model. Two aromatic residues in the S6 helix lining the intracavitary site that are most commonly associated with high-affinity blockade of hERG1 are Y652 and F656. Both residues are established as a critical determinant of hERG1-induced block associated with proarrhythmia (Ficker et al., 1998; Lees-Miller et al., 2000; Mitcheson et al., 2000; Perry et al., 2010). Recent work of Saxena et al. (2016) emphasized an important role for another aromatic residue (F557) from the S5 helix. It was shown that F557 may be involved in the drug stabilization of hERG1 binding pocket along with the residues in the S6 helix. Therefore, we chose to include F557X along with classic aromatic cassette Y652X and F656X to screen for ivabradine binding to the well established intracellular site.

As for the M651 mutation, previous blinded docking studies showed the presence of a potential binding domain for ivabradine in close proximity to this residue, only in the open state of the channel (Lees-Miller et al., 2015). However, no electrophysiological experimental data on M651X mutants was reported in the previous report. The MD simulations also showed a favorable energetic partitioning of the neutral state ivabradine into the lipid bilayers. The comparison of in-silico models used by Lees-Miller et al. (2015) to the recently solved cryo-EM structures showed that the key structural elements in the pore domain (S5–S6) were accurately captured by ROSETTA-generated models of hERG1 (RMSD $< 3.5 \text{ \AA}$) (Wang et al., 2016) providing additional support for docking studies on hERG1 models. In this study we created the M651T mutation to examine its effects on ivabradine binding (Fig. 2). We reasoned that the substitution of methionine by the small polar amino acid (threonine) at the M651 site could disrupt the lipophilic binding or access route of ivabradine. We discovered that M651T expressed well in cells but the mutation slowed deactivation kinetics of the channel and suppressed the block induced by ivabradine (Fig. 2). This raised a possibility that

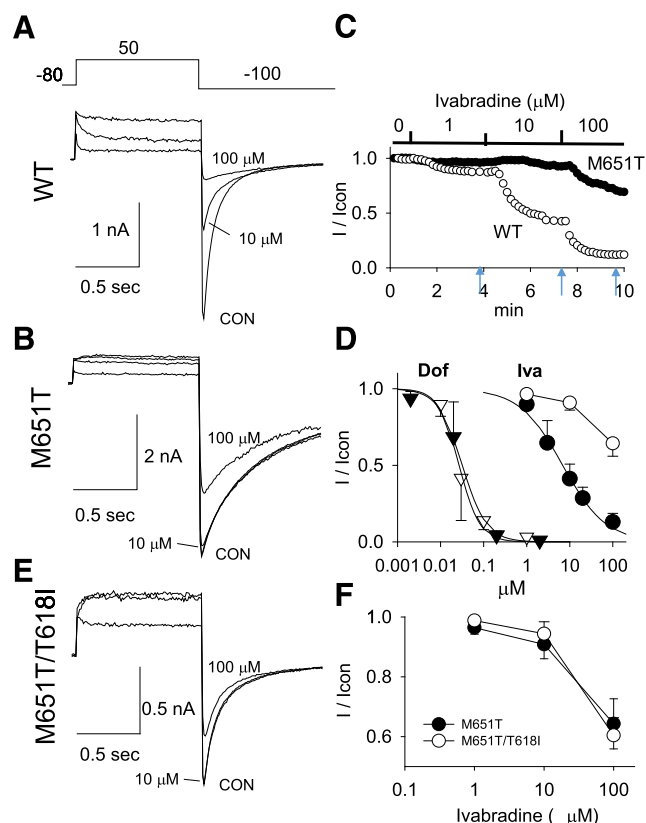


Fig. 2. Effect of ivabradine on WT-hERG1 (A) and M651T-hERG1 currents (B), respectively. (C) The representative time-courses of the WT and M651T current in response to application of various concentrations of ivabradine. The original current traces (times indicated with arrows) were shown in (A) and (B). (D) The dose-response curves of dofetilide (triangles) and ivabradine (circles) blockade of M651T-hERG1 (open symbols) and WT-hERG1 currents (solid symbols). For all experiments with ivabradine blocking M651T-hERG1, $n = 3, 6, 7$ for concentrations of drugs 1, 10, and 100 μM , respectively. For ivabradine block of WT-hERG1, $n = 5$ was used for every concentrations. The dose-response curves of dofetilide block of M651T-hERG1 were obtained with $n = 5, 7, 5, 10$ with concentrations of 0.01, 0.03, 0.1, 1 μM . For dofetilide block of WT-hERG1, $n = 1, 3, 2, 2, 5$ in the concentrations of 0.002, 0.02, 0.1, 0.2, 2 μM . (E) Effect of ivabradine on M651T/T618I hERG1 currents. (F) The dose-response curves of ivabradine blockade of M651T/T618I hERG1 in comparison with blockade of M651T-hERG1. All experiments for M651T/T618I-hERG1 system were performed with $n = 3$.

M651T modifies ivabradine-induced block by altering the deactivation time-course of the channel. To account for this covariable and to directly address whether the slowing of deactivation contributed to the shift in the concentration-response relationship to ivabradine, we created a double mutation, M651T/T618I. The rationale for its creation relates to a previous study wherein we reported that T618I accelerated deactivation kinetics. We empirically created the double mutation M651T/T618I to restore deactivation to WT values while retaining the key M651T substitution.

Mutations of Lipid-Facing Residue M651 Significantly Alters Thermodynamics and Kinetics of Ivabradine. Figure 2, A and B, show raw data of the concentration-dependent ivabradine-induced block of WT hERG1 (Fig. 2A) in comparison with the M651T mutant (Fig. 2B). Figure 2C shows a representative time-course of block of I_{hERG1} by ivabradine at various concentrations. I_{hERG1} designates the I_{Kr} -like current elicited by transfecting the HEK cells with the hERG1 cDNA construct. Figure 2D shows the

mean concentration-induced block comparing ivabradine (open circles for the WT, closed circles for the M651T) to dofetilide (open triangles, WT, and closed triangles, M651T; n values are shown in the legend). At 10 μM ivabradine suppressed 75% of the WT current, whereas at the same concentration, the drug blocked only 10% of the M651T current (Fig. 2D). The mean IC_{50} was $6.5 \pm 10 \mu\text{M}$ for ivabradine in WT ($n = 10$), for M651T the IC_{50} was $>120 \pm 10 \mu\text{M}$ ($n = 7$), and beyond the drug's solubility limit. Note that to accurately measure IC_{50} , a concentration higher than its solubility limit is essential. The impact of the lipid-facing residue M651 to ivabradine was also compared with dofetilide, a prototypical class III antiarrhythmic drug, to assess whether the mutant had a greater impact on response to ivabradine.

Interestingly, the M651T mutation had no impact on the concentration-response relationships to dofetilide. The mean IC_{50} concentration for dofetilide in WT was 41 nM ($n = 4$), whereas it was 27 nM for the M651T mutation ($n = 5$). Thus, the M651T alters the concentration-response relation for ivabradine but not for dofetilide.

The stark contrast in the drug sensitivity for a lipid-facing mutation suggests that the two drugs are accessing the main intracavitary site of hERG1 via different pathways. The pK_a values reported for the strongest basic chemical moiety in ivabradine (9.37) is similar but somewhat lower than of dofetilide (9.6). Nonetheless, the cationic form of the drug is a dominant form in the bulk aqueous solution at the physiologic pH values. However, the pK_a values of weak-cationic compounds such as ivabradine are not the most accurate predictor of partitioning thermodynamics, since the equilibria between a neutral and a cationic form is a dynamic and environment-dependent process (DeMarco et al., 2018; Dickson et al., 2019).

To investigate thermodynamics of partitioning between aqueous phase and a model hydrophobic environment that mimics the membrane bilayer interior, we studied partitioning of ivabradine and dofetilide in an aqueous buffer and n -hexane. The thermodynamics of transfer for the two drugs showed significant differences. The partitioning free energy data summarized in Table 1 directly demonstrate that ivabradine has probabilities of partitioning nearly equal between aqueous buffer and a bulk hexane (Table 1). The free energy of transfer (ΔG_{tr}^0) between aqueous phase and a bulk hexane for $T = 313.15 \text{ K}$ are 0.5 ± 0.1 and $8.4 \pm 0.2 \text{ kJ mol}^{-1}$ for ivabradine and dofetilide, respectively. Therefore, partitioning data provide direct evidence that ivabradine is a lipophilic molecule, which partitions into the lipid compartment of the plasma membrane compared with dofetilide (Table 1). These findings are in excellent agreement with our previously published modeling studies (Lees-Miller et al., 2015).

Although M651T Slows Deactivation, Its Impact on Ivabradine-Induced Block Appears Independent of Deactivation. In comparison with WT, M651T mutation slows deactivation; the τ s of WT hERG1 and the mutant were 160 ± 40 and 400 ± 40 milliseconds ($P < 0.01$), respectively. Figure 2, A, B, and E, show the raw deactivation time-course in response to ivabradine in WT (Fig. 2A) and M651T (Fig. 2B) and in a double mutation which rescues deactivation to the WT values (Fig. 2E). Figure 2B shows the drug free time course of deactivation of the M651T mutation compared to the WT (Fig. 2A). The double mutant channel, M651T/T618I restored the deactivation time-course of the channel to values similar to WT hERG1 (compare Fig. 2, A, B, C, and E), both drug-free and with ivabradine. Even the double

TABLE 1

Mole fractions (x_S) and associated thermodynamic parameters for dofetilide and ivabradine hydrochloride partitioning in buffer-hexane system at $T = 298.15$ and 313.15 K , $\text{pH} = 7.4$, and pressure $P = 0.1 \text{ MP}$

	Temperature	Buffer	Hexane	Log $D_{H/B}$	ΔG_{tr}^0
	K	$x_B \cdot 10^6$	$x_H \cdot 10^6$		$\text{kJ} \cdot \text{mol}^{-1}$
Dofetilide	313.15	5.38	0.215	-1.40	8.4 ± 0.2
	298.15	5.34	0.258	-1.32	7.9 ± 0.2
Ivabradine	313.15	3.55	2.93	-0.08	0.5 ± 0.1
	298.15	3.69	1.67	-0.34	2.0 ± 0.1

mutant of the hERG1 channel that contains M651T still shifted the IC_{50} concentration-response of ivabradine by more than two orders of magnitude (Fig. 2F). The mean IC_{50} values of M651T were nearly identical to that of the double mutation M651T/T618I (Fig. 2F). These data indicate that decreased pharmacological sensitivity to ivabradine was not the result of slowing deactivation kinetics induced by the M651T mutation.

Impact of Other M651X Substitutions on Ivabradine-Induced Block. The relationship between baseline drug-free electrophysiological characteristics and IC_{50} values were evaluated by creating various substitutions at the M651 site (Supplemental Figs. 1–4). We sought to address whether there was a relationship between electrophysiological characteristics and IC_{50} response to ivabradine. We observed no significant correlation between drug-free voltage-dependence of activation ($V_{1/2}$), deactivation kinetics, or voltage-dependence of C-type inactivation and the concentration-responsiveness to ivabradine. However, there was a modest correlation between the drug-free time-constant of recovery from inactivation and the mean IC_{50} values of ivabradine-induced block ($R^2 = 0.4$). We next examined the effect of an IC_{50} concentration of ivabradine on ion currents elicited in various substitutions at the M651 site. The voltage-dependence of deactivation (during ivabradine treatment) and the kinetics of recovery from inactivation and their associated IC_{50} values were significant, but these correlations were quite modest. Although many substitutions at this lipid-facing residue (Supplemental Table 2) have significant impact on responsiveness to ivabradine, correlation between “the lipophilicity of the residues” and the mean IC_{50} values for ivabradine block was limited or even absent ($R^2 < 0.1$ – 0.4). There were no apparent correlations between the IC_{50} for ivabradine binding or volume or solvent-accessible area of the residues in the 651 position (Supplemental Fig. 3). It is important to mention that in the absence of ivabradine, several of the M651X mutants exhibited altered gating behavior (Supplemental Figs. 3 and 4).

Therefore, ivabradine-induced block of hERG1 current could not be reduced to a simple drug binding in the vicinity of M651X. The drug action may be coupled to the gating process of the channel or altered accessibility to the intracellular cavity of the channel via some form of allosteric regulation. Essentially, drug-induced shifts in the time-course of recovery from inactivation appear to be a probable determinant of ivabradine potency. This coupling between presence of binding pockets, drug-channel interactions at the lipid-facing surface, and gating dynamics is often described in terms of a complex allosteric mechanism in which change in the topology of the binding pocket or inter-residue interactions modulates access or affinity for the substrate binding pocket (Gordon and Zagotta, 1995).

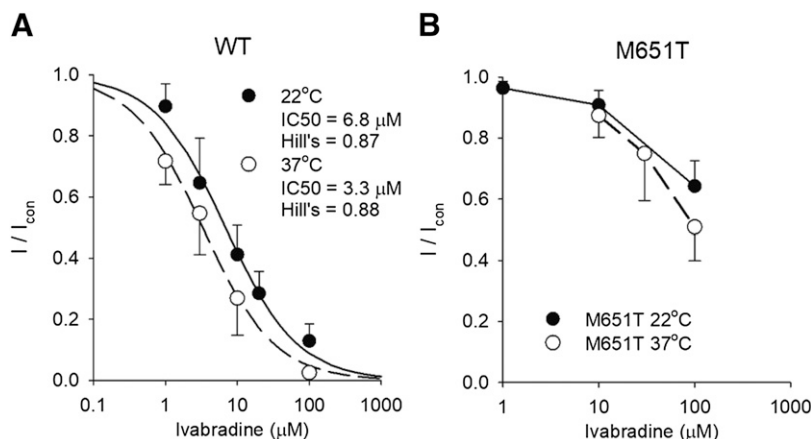


Fig. 3. The temperature dependence of the concentration-response curves for ivabradine blockade of WT-hERG1 (panel A) and M651T-hERG1 (panel B) currents at $T = 22^\circ\text{C}$ and 37°C shown as closed and open circles, respectively. In the WT-hERG1 experiments at $T = 22^\circ\text{C}$, n were 6, 5, 5, 5, 5 for concentrations of 1, 3, 10, 20, 100 μM of ivabradine. $T = 37^\circ\text{C}$, $n = 8, 7, 3, 4$ for drug concentrations of 1, 3, 10, 100 μM , respectively. In the M651T construct at $T = 22^\circ\text{C}$, $n = 3, 6, 7$ for experiments performed with 1, 10, 100 μM , respectively. At $T = 37^\circ\text{C}$ $n = 4, 3, 5$ for 10, 30, 100 μM , respectively.

Temperature Dependence of Ivabradine Blockade.

The measured IC_{50} values for ivabradine in WT hERG1 differ somewhat between various laboratories. We note that our originally published IC_{50} value of 6.8 μM differs from that of Melgari et al. (2015). Their measurements were reported at 37°C , whereas our measurements were made at 22°C . Accordingly, to address whether experimental conditions accounted for some of these differences in measured IC_{50} values we directly compared IC_{50} values of ivabradine at 37°C versus 22°C . Our measured wild-type IC_{50} value at 37°C of 3.3 μM is relatively close to the values of 2.07 μM for hERG1 and 3.31 μM for WT-hERG1 1a/1b isoform reported by Melgari et al. (2015). Most importantly, we further re-established that the impact of M651T was not significantly altered by increasing the temperature to 37°C (Fig. 3B). In fact, higher temperature may induce more potent block by ivabradine. The measured IC_{50} of ivabradine decreased from 6.8 to 3.3 μM with an increase in temperature, paralleling more favorable partitioning of ivabradine into the hexane at a higher temperature (Fig. 3; Table 1). Given that ivabradine is a highly lipophilic compound, the drug precipitates at higher concentrations as in these experiments, thereby making it impossible to calculate an exceedingly accurate IC_{50} value for ivabradine block of M651T, because the solubility of ivabradine prevents evaluations at concentrations $>100 \mu\text{M}$.

Interplay Between Aromatic Cassette (Y652, F656, and F557) Dynamics and Ivabradine-Induced Block. A vast number of studies describing molecular determinants of high- to mid-affinity blockade have emphasized an important role played by aromatic residues in the pore-domain cavity of the channel (Y652 and F656) (Duff et al., 1995; Ficker et al., 1998; Lees-Miller et al., 2000, 2015; Mitcheson et al., 2000; Perry et al., 2010; Saxena et al., 2016). These residues are pivotal determinants of class III drug-induced block of I_{hERG} ; thus a range of double mutations were created to enhance our understanding of the interplay between those key residues in the pore domain and the lipid-facing residue M651 (Ficker et al., 1998; Lees-Miller et al., 2000; Mitcheson et al., 2000; Perry et al., 2010; Saxena et al., 2016). Figure 4 shows the pharmacological responses of ivabradine to the single and double mutations. Figure 4, A–C, show the effects of adding the M651T mutation to F656C, Y652, or S620T. S620T is a mutant with impaired C-type inactivation phenotype (Herzberg et al., 1998; Perry et al., 2007) that also has a major impact on channel-induced activation or block by small

molecules (Ficker et al., 1998; Herzberg et al., 1998; Wu et al., 2014, 2015). We previously reported that the single mutation S620T decreases the pharmacologic responsiveness of I_{hERG1} to ivabradine (Lees-Miller et al. 2015).

A large concentration of ivabradine (100 μM) only partially blocks the F656C (72% block), Y652A (30%), M651T (30%), and S620T currents (32%), but almost no block was observed at the same concentration of ivabradine with either the M651T/F656C ($<1\%$ block), M651T/S620T (1% block), or M651/Y652A (12%) compared with their respective individual mutations as seen in Fig. 4 (P and n values are shown in the legend and statistical analysis of the data are provided in the Supplemental Table 1). The analysis of electrophysiological recordings in Fig. 4 show no additive or synergistic interplay between F656 and Y652 (Fig. 4E). These data indicate that the M651 site substantially modifies the impact of known aromatic mutations in the distal S6. Mutations of F557L and M651T, both, impaired ivabradine-induced block, but surprisingly the block of the double mutant F557L/M651T was similar to the WT values (Fig. 4D and the raw data are shown in Fig. 5A,B). Panel A shows the raw data before and after ivabradine addition. Panel B shows the mean IC_{50} concentration-response plots. Panel C shows the washout. These data indicate F557 in the S5 and M651 in the distal S6 negatively interplay to rescue pharmacologic response of ivabradine. However, no significant negative or positive interplay is observed with single or double mutations of F557L and S620T (Fig. 4F). In review, the M651 residue interplays positively with many other key residues that are structural determinants of ivabradine-induced block. In contrast, M651T interplays negatively with F557L (Fig. 5B). These data suggest a presence of a complex allosteric interaction of ivabradine with residues in hERG1—a novel mechanism established in this work.

Discussion

State-Dependence in the Ivabradine Blockade of hERG1 Currents. One of the most important determinants of hERG1 block-associated proarrhythmia is the state-dependent kinetics of drug interactions with the channel (Di Veroli et al., 2013a, 2013b; Hill et al., 2014). The landmark feature of hERG1 channel kinetics is the rapid C-type inactivation (Sanguinetti et al., 1995; Schönherr and Heinemann, 1996; Spector et al., 1996). A number of mutations significantly

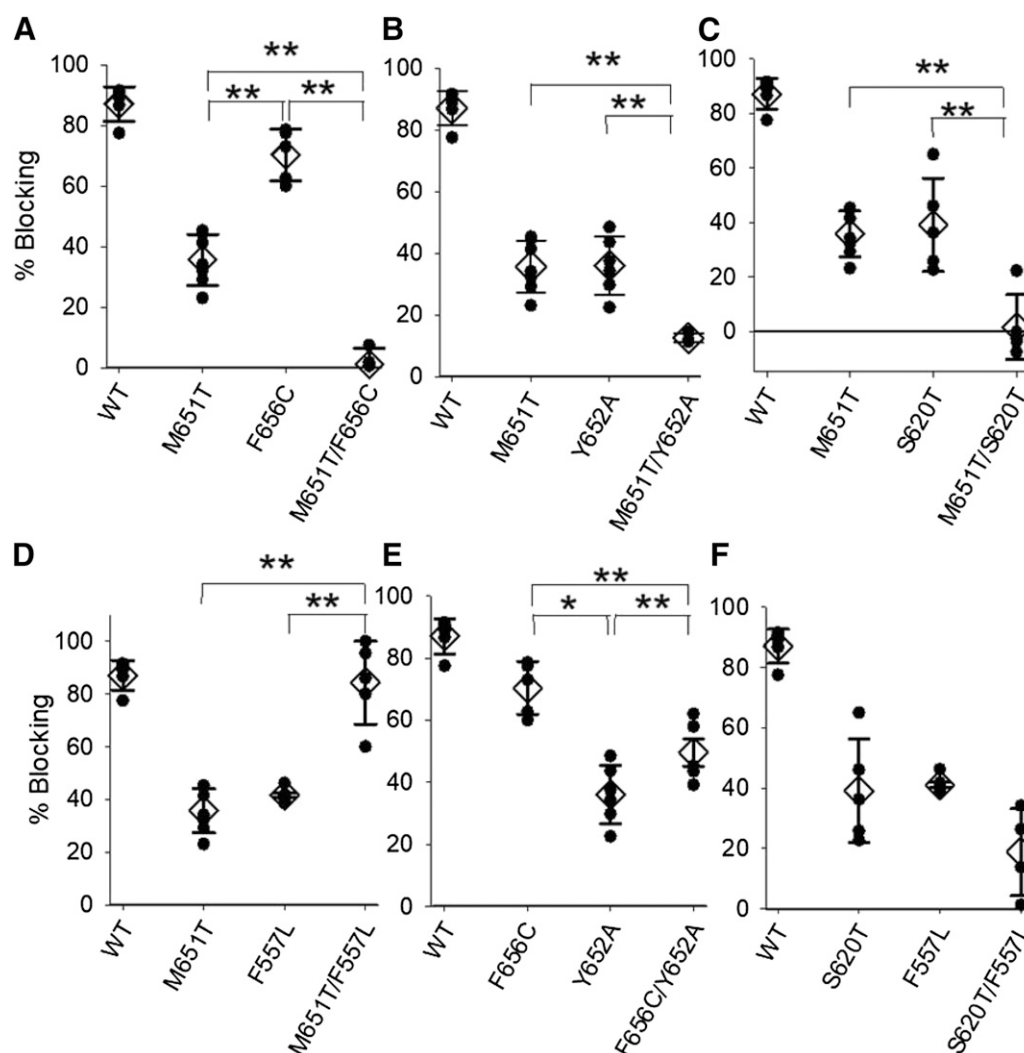


Fig. 4. Analysis of concomitant interactions of double mutations in blocking effects of saturating concentration of ivabradine (100 μ M). Blocking effect of (A) M651T/F656C, (B) M651T/Y652A, (C) M651T/S620T, (D) M651T/F557L, (E) F656C/Y652A, (F) S620T/F557L, and their corresponding single mutations are shown. The following number of experiments was used: $N = 5, 7, 5, 4$ in order of in (A); 5, 7, 6, 3 in (B); 5, 7, 5, 5 in (C); 5, 5, 6, 5 in (D); 5, 5, 5, 4 in (E); 5, 5, 5, 4 in (F). * $P < 0.05$; ** $P < 0.01$. One way ANOVA analysis was used. The precise statistic P values are provided in the Supplemental Table 1. WT was used as reference and was not included in the statistical analysis.

alter or shift the voltage-dependence of C-type inactivation, including the S620T mutant. Therefore, the contribution of inactivation of M651T mutation on ivabradine-induced block was assessed by comparing the extent of block in M651T, S620T, and the double mutant M651T/S620T. By combining a noninactivating pore (S620T) with the M651T mutation, drug block was virtually eliminated. These data indicate that both the process of C-type inactivation and the M651 site in the distal S6 interact to produce at least additive impairment of ivabradine-induced block. Collectively, the results described for mutations in the positions F557, M651, Y652, and F656 indicate that drug blockade depends on the coupling between conformational dynamics of the residues in the pore domain and on a mechanism that involves repacking of the lipid- and/or pore-facing residues. How are state-dependent conformational dynamics of F557, M651, Y652, and F656 coupled to drug access/binding to a pocket? To understand dynamics of these residues we performed 1.2- to 2.5-microsecond all-atom molecular dynamics simulations in an explicit water/membrane system for selected mutants.

Orientations of F557 and F656 are State-Dependent Properties: From Pore-Lining to Lipid-Facing. The availability of new cryo-EM structures for hERG1 and hEAG1 channels in combination with recent developments in MD simulations allowed us to investigate structural dynamics of the open and closed states along with mutants of interest, hence allowing us to test directly the hypothesis presented above. In the previous and widely accepted mechanistic models, the aromatic residues (Y652 and F656) were postulated to face the permeation pathway and coordinate drugs bound to the intracellular cavity (Chen et al., 2002; Perry et al., 2010). Various structural models with bacterial K^+ channels or Shaker-family of K^+ channels as their bases emphasized the importance of direct interactions between drugs bound in the water-filled cavity with F656 and/or Y652 (Perry et al., 2010; Wacker et al., 2017). The recent progress in cryo-EM technologies allowed us to model open and closed states of hERG1 channel. Although the model based on hEAG1 represents a closed pore, a cryo-EM structure for hERG1 corresponds to the open state. Importantly, spatial

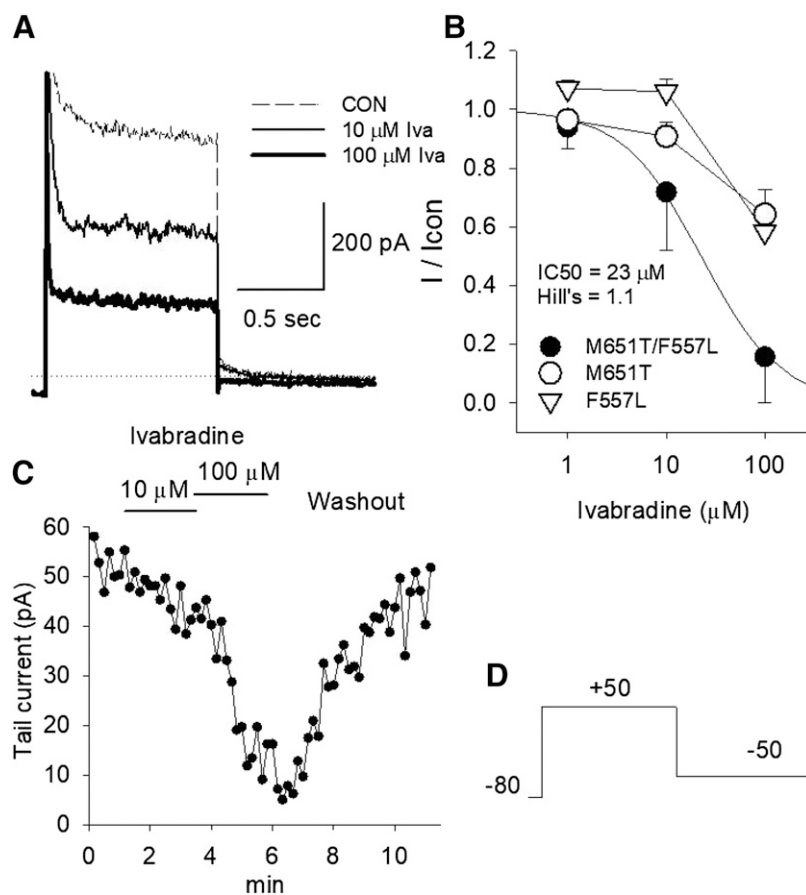


Fig. 5. Current traces (A) and time-course (C) of ivabradine on M651T/F557L and their single mutations. (C) The concentration-response curves. The smooth curve was fitted to the Hill equation. Fitting of M651T and F557L was not possible. (E) The following numbers of experiments were performed: $N = 3, 4,$ and 5 in F557L; $n = 3, 6,$ and 7 in M651T; $n = 4, 5,$ and 5 in M651T/F557L in concentrations of $1, 10,$ and 100 mM, the legend is shown on the figure. (D) Patch-clamp protocol.

orientation of F656 and F557 side-chains display remarkable state dependence. As predicted by a majority of structural modeling studies, the F656 is pointing toward the inside of the cavity in the closed-state model (Wang et al., 2016; Wacker et al., 2017)). All-atom MD simulations indicate that F656 can rotate away from the permeation pathway and in the open-state model flickers between the intracavitary and the lipid-facing orientations (Fig. 6, A–C). In the open state, the position of F656 aromatic ring is in proximity to F557 and is close enough to form stable π - π stacking interactions at the lipophilic entry pathway.

To assess properties of the putative lipid-entry pathways and the impact of various mutations on the dynamics of the F557-M651X-F656 motif, we performed topological analysis of the production portion of MD simulations (for traces, see Supplemental Figs. 5 and 6) using the MOLEonline pathway analyzer (Berka et al., 2012). Two potential entry pathways were mapped from analysis of MD trajectories. Both pathways are defined by conformational states of F656 and F557 residues and illustrated in Fig. 6A. We analyzed the conformational dynamics of the F557-F656 pair to gain additional insight regarding the flexibility of a tentative lipid-facing binding site and its impact on the accessible volume required for drug diffusion into the primary intracavitary site (Supplemental Fig. 5). The conformational space of F557-F656 interacting pair and the impact of M651T mutation in different states of hERG1 is illustrated in Fig. 6, B–D. The direct interactions between F656 and F557 appear to be only quasi-stable (flickering state) in the WT hERG1 (Fig. 6, B, C, D, E). These interactions establish a large accessible volume

for drug binding on the lipophilic site of the intracellular cavity. The interaction of the pair is state-dependent, which may directly support the previously postulated role of F656 in the state-dependent drug blockade of hERG1 channel (Chen et al., 2002). Therefore, it is tempting to assign the F656-F557 pair a pivotal role in state-dependent gate control of ivabradine diffusion from the lipid bilayer to the main binding site in the intracellular cavity. The additional analysis of M651T mutant shows that the conformational flexibility of the F656 and F557 pair is significantly impeded with the mutant (Fig. 6C, D, E). Evidently, the M651T mutation significantly stabilizes the pair (F656 and F557) by decreasing the F656 “flickering” frequency (Fig. 6, B and C). Other mutations affecting conformational flexibility of F656 or F557 (Supplemental Figs. 7–14) are also associated with inhibition of hERG1 blockade by ivabradine. The structural states of F656 appear to be important modulators of high-affinity binding for major hERG1 blockers (Supplemental Fig. 14; Supplemental Table 4).

In review, the state-dependent orientation of F656 appears to be an important determinant of a putative lipophilic entry pathway explored by some of the hERG1 blockers, including ivabradine. The all-atom MD-refined models of hERG1 channel in its open and closed states demonstrate that F656 can rotate away from the intracellular cavity toward the lipid bilayer and form hydrophobic interactions with F557 and M651 residues (Fig. 1). Interestingly, the conformational flexibility of F656 (it can be directly modulated by mutations in the position M651 or F557) is in excellent correlation with findings observed experimentally in ivabradine blockade to WT and mutant forms of hERG1.

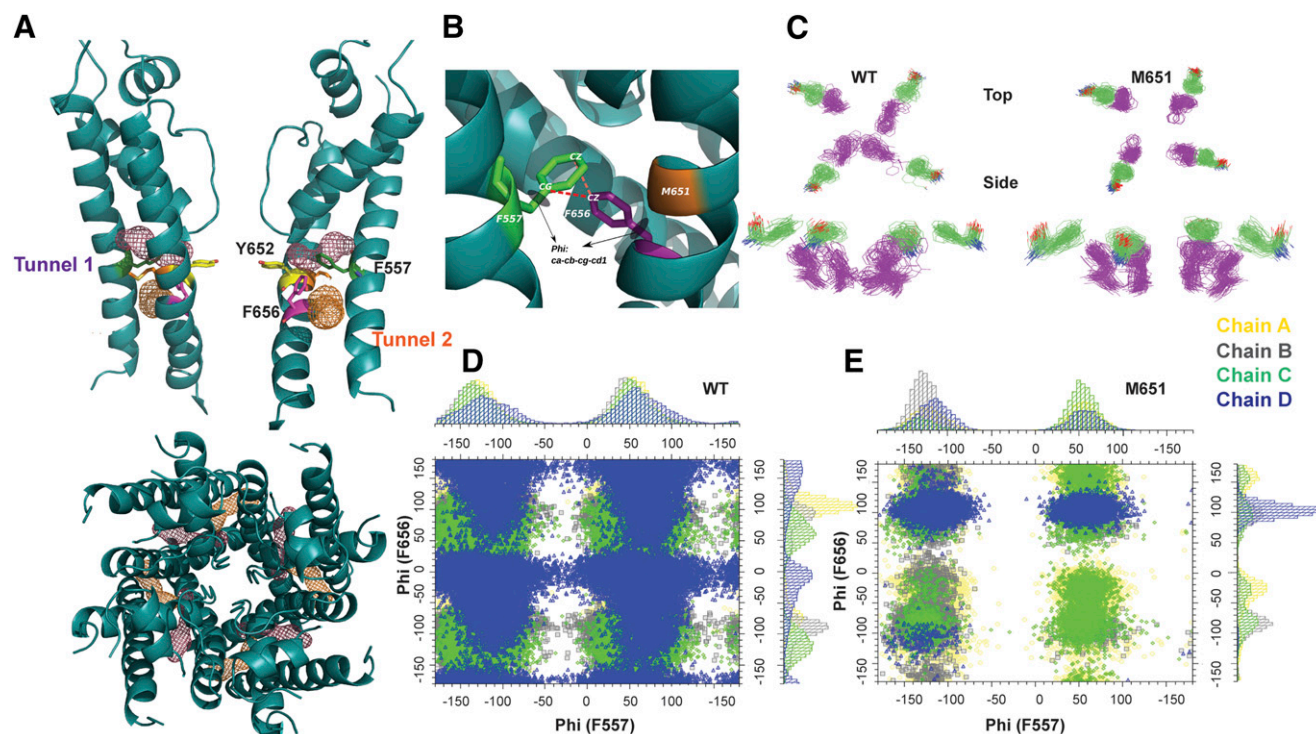


Fig. 6. Impact of the M651T mutation on the conformational dynamics of aromatic cassette in WT-hERG1 and M651T-hERG1 systems. The dihedral distributions and accessibility mapping were obtained from the last 750 nanoseconds of equilibrium all-atom MD simulations. (A) Side view of two subunits and top view of the pore domain showing relevant access pathways mapped by the MOLLonline tool (see Supplemental Information for details). Selected residues are shown: F557 (green), F656 (magenta), M651 (orange), and Y652 (yellow). (B) Key distances and torsional angles involving F557 (green sticks) and F656 (magenta sticks). Position of residues M651 in the S6 helix are colored in orange. (C) Top and side views of the superimposed positions of F557 (green) and F656 (magenta) for WT-hERG1 (left) and M651T-hERG1 (right). (D and E) one-dimensional and two-dimensional distribution maps for torsional angles in each subunit of WT-hERG1 (D) and M651T (E). One-dimensional distributions are shown for F557 (top panel) and F656 (side panel), respectively.

Induced-Fit Docking and MD-Ensemble Docking Supports Coexistence of Binding Sites in the Pore Cavity and Pore-Lipid Interface. The extensive sampling of various conformational states of WT and mutant forms of hERG1 channel in different states achieved with Anton 2 platform allowed us to map tentative binding sites for ivabradine. Potential binding sites around the mutated residues were explored through docking of ivabradine to different sections of the protein using hERG1 in different states, also incorporating ensemble docking, where cluster-representatives from all-atom MD simulations were used. Two main binding sites, “lipophilic site” and “internal cavity site,” were further analyzed and compared for WT hERG1 and mutants. The stable and populated binding sites from Induced-Fit Docking are shown in Fig. 7, and a summary of docking energetics for all studied systems are shown in Tables 2 and 3. There were no poses found for ivabradine binding (either neutral or cationic form) to the main internal cavity of the hERG1 for the closed state of the receptor (Table 2). For the closed state of hERG1, ivabradine shows stable binding to the pocket centered at M651, in agreement with the previously proposed lipophilic access site (Lees-Miller et al., 2015) (Table 2). In contrast to the closed state of the channel, the docking to the open state revealed three stable binding modes. Ivabradine was favorably bound to the main pocket in the intracellular cavity, to an area around a fenestration window (in-between α -helices of S6), or to a lipid-facing binding pocket (Fig. 6A). The IFD docking performed to an open state of the hERG1 channel or the MD simulations to an ensemble of open

structures show similar binding affinities for ivabradine (Table 3). The results of IFD docking qualitatively agrees with the experimental data (Table 2). At the same time, results from the MD-ensemble docking inherently have large uncertainties in computed binding affinities, rendering comparisons between mutants rather difficult (Table 3). However, the ensemble-based docking simulations allow for better quantification and comparison of relative populations found in each of the three binding sites. The population analysis is essential for understanding the binding processes that involve large and flexible ligands such as ivabradine (Zhao et al., 2010; Shoichet and Kobilka, 2012). The relative populations of binding poses found for identified sites are shown in Fig. 7 and Table 3. Comparing number of poses from the docking simulations, ivabradine preferentially binds to the lipophilic site or the internal cavity of the WT hERG1. However, a substantial number of poses are also found near a potential fenestration window or the “access pathway” (Fig. 7A; Supplemental Fig. 6).

For additional insights, we performed docking simulations on selected mutant systems, specifically M651T, F557L, and F557L/M651T hERG1 mutants. It was found that in both M651T and F557L mutants, ivabradine showed a preferential binding to the intra-cellular cavity of the channel and a very small occupancy (number of poses) in the lipophilic binding pocket. In conclusion, ensemble docking for both mutants M651T and F557L indicate disruption of the lipophilic access site owing to the repacking of this binding pocket caused by the mutations. The mutations in 651 and 557 reduced relative

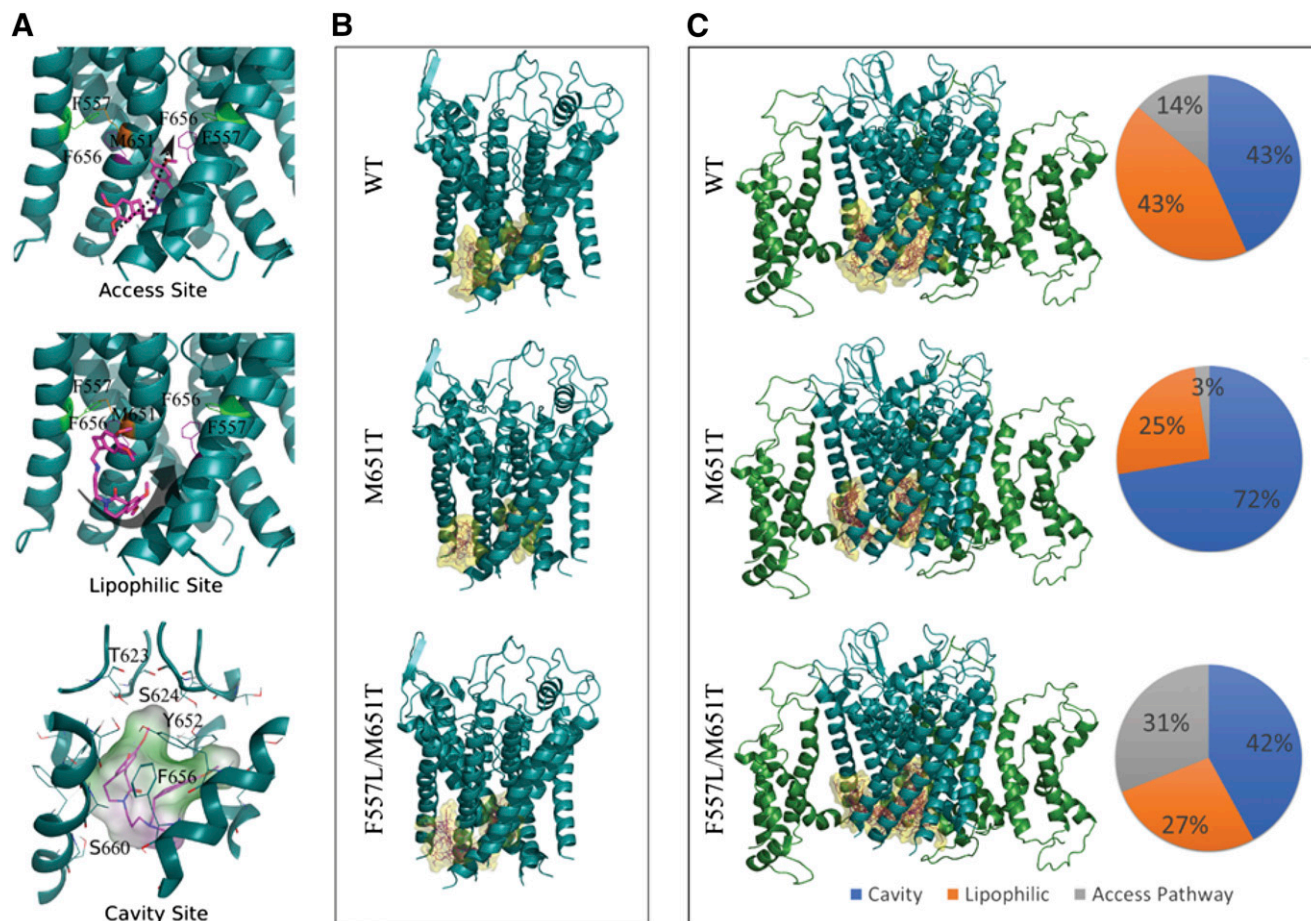


Fig. 7. Molecular docking of ivabradine to different sites of the pore domain (PD) and the transmembrane domain (TMD). (A) Induced-Fit Docking (IFD) of ivabradine to PD access site (top), lipophilic site (middle), and intracellular cavity site (bottom). Ivabradine is shown in magenta and relevant interacting residues are labeled. The arrows indicate the potential access route that the drug might follow to access the cavity and produce the block. (B) Ensemble of binding poses mapped from the IFD docking showing the exploration of the different binding sites for WT (top), M651T (middle), and F557LM651T (bottom) in the PD of hERG1. No poses were found in the access path site for M651T. (C) Group of poses found by MD-ensemble docking showing the exploration of the different binding sites for WT (top), M651T (middle), and F557LM651T (bottom) TM hERG1. Results involving only one of the four subunits are shown for clarity. Results for all subunits are displayed in the corresponding pie charts beside each system and in Table 3. In agreement with IDP docking performed with cryo-EM structure, almost no poses were found on the access path site for M651T mutant.

population of binding poses in the binding pocket near a potential fenestration window (access path to the internal cavity path) by 2-fold compared with the WT system. These findings are in excellent agreement with the electrophysiological data presented herein. The data combined for the double mutant M651T/F557L indicate almost WT-like binding affinities in all three mapped binding sites with modest increase in binding affinity for intracellular cavity- and the access binding sites (Fig. 7C). Therefore, the double mutant is expected to have WT-like binding properties in the open state of the channel. We conclude that the flexible nature of F656 side-chain, which can rotate toward the lipid-facing side and the internal cavity of the channel seems to be a determining factor in ivabradine-induced block. MD simulations have also shown that the double mutant F557L/M651T restores the WT-like dynamic of F656 flickering, therefore re-establishing drug occupancy in the lipophilic access site for ivabradine. Subsequent ivabradine docking to WT hERG1 and selected mutants (M651T, F557L, and F557L/M651T) indicated that the lipophilic site is accessible to both open and closed states of the channel. However, the closed state of the channel contains no binding pockets for ivabradine in the intracellular cavity and

the “access” binding site near the fenestration window. The simulation data suggest that the structural rearrangements of this binding pocket during the channel’s activation may play a role in ivabradine binding to the lipophilic site and subsequent access to the entry site and ultimately into the intracellular cavity of the channel. Molecular docking simulations

TABLE 2

Binding affinities of ivabradine docking to hERG1 pore-domain models. Binding affinities of the best pose for WT and mutants are shown. Docking boxes were defined around the centroid of residues F557 and M651.

PD System	Closed hERG1 Model 20 Å Box, BE		Open hERG1 Cryo-EM Model 15 Å Box, BE	
	Lipophilic	Cavity	Lipophilic	Cavity
	<i>kcal/mol</i>		<i>kcal/mol</i>	
WT ^a	−5.45	No Poses	−7.36	−8.59
F557L/M651T ^a	−5.05		−6.76	−8.89
M651T ^s	−4.84		−4.56	−7.95
F557L	−4.96		−5.44	−7.84

^aPoses in the access path to internal cavity were found, see Fig. 4, Supplemental Fig. 3, and Supplemental Table 3.

TABLE 3

Ivabradine affinity to hERG1 transmembrane domain from GlideXP docking to the selected MD frames of WT and mutant hERG1

Poses were clustered into three binding sites: cavity, lipophilic, and “access path.” Average energy considering all four subunits is presented as kilocalories per mole as well as the percentage of poses found within the binding site.

TM System	hERG1 Cryo-EM Model		
	Cavity	Lipophilic	Access Path
	kcal/mol	kcal/mol	kcal/mol
WT	-5.22 ± 1.45 (43.2%)	-4.72 ± 0.93 (43.1%)	-4.42 ± 0.93 (13.7%)
M651T	-5.71 ± 1.31 (72.1%)	-4.58 ± 0.74 (25.3%)	-4.19 ± 1.40 (2.6%)
F557L	-5.57 ± 1.27 (67.2%)	-4.75 ± 0.89 (26.6%)	-4.27 ± 0.72 (6.1%)
F557L/M651T	-4.69 ± 1.10 (41.8%)	-4.76 ± 0.99 (27.3%)	-5.00 ± 1.08 (30.9%)

performed for the cationic form of ivabradine targeting primary site in the intracellular cavity show comparable binding free energies (to the lipophilic site) and also underline the crucial role of F656 dynamics (Supplemental Table 4) coupled to the complex interactions with F557 and M651 residues.

Conclusions

In summary, we show that the pore-lipid interface mutation (M651T) significantly impairs ivabradine-induced block of the hERG1 current but does not alter dofetilide-induced block. Thus the impact of M651T appears to be specific to ivabradine and emphasizes the underlying important role of a new lipophilic access pathway. The structural mechanisms of the observed lipophilic binding of ivabradine were discerned from a combination of microseconds-long MD and traditional IFD/MD-ensemble docking simulations. The modeling data emphasize the role of M651 as an allosteric modulator of state-dependent hydrophobic interaction between F557 and F656, both of which are well known determinants of ivabradine-induced block. The F557 residue was shown to interact with F656 by forming π - π stacking interactions, an interaction that is disrupted by M651. The overall process of M651 tugging on F656 results in a mobile and flickering F656, which flickers to face the lipid-facing side and the internal cavity. Whereas M651T mutant is unable to interact with F656, it enhances F656 and F557 π - π stacking interactions, resulting in a rigid F656. Thus, M651 controls the quasi-flickering state of F656 and shapes the topology of the binding pocket by controlling orientation of the F656/F557 hydrophobic cassette. MD simulations provided direct evidence that the mutations at these two positions (F557 and M651) cause changes in the topology in the vicinity of the proposed access and/or lipophilic binding sites by altering F656 flexibility and rotations, thereby impacting the number of binding poses and hence limiting accessibility to the main binding pocket in the intracellular cavity of the open-hERG1. We conclude that in WT-hERG1 channel F656, M651, F557 residues act as a dynamic gate that controls the pathway of drug access at the lipid-facing domain into the intracellular cavity of the channel. The experimental data provided firm evidence that the extent of ivabradine blockade recorded for F557L/M651T mutant with WT-like conformational dynamics was essentially similar to the WT hERG1.

Acknowledgments

We thank Dr. Marcela Madrid and Dr. Philip Blood of Pittsburgh Supercomputing Center for their assistance with running molecular

dynamics simulations on Anton 2 platform. We express our gratitude to Martin Karplus and CHARMM project for waiving license fees for the CHARMM program package used for analysis of simulation data.

Authorship Contributions

Participated in research design: Perissinotti, Guo, Lees-Miller, Noskov, Duff.

Conducted experiments: Perissinotti, Guo, Kudaibergenova, Ol'khovich, Sharapova, Perlovich.

Contributed new reagents or analytic tools: Guo, Muruve, Gerull, Noskov, Duff.

Performed data analysis: Perissinotti, Guo, Kudaibergenova, Noskov, Duff.

Wrote or contributed to the writing of the manuscript: Perissinotti, Guo, Kudaibergenova, Muruve, Gerull, Noskov, Duff.

References

- Abi-Gerges N, Holkham H, Jones EM, Pollard CE, Valentin JP, and Robertson GA (2011) hERG subunit composition determines differential drug sensitivity. *Br J Pharmacol* **164** (2b):419–432.
- Bender BJ, Cisneros A III, Duran AM, Finn JA, Fu D, Lokits AD, Mueller BK, Sangha AK, Sauer MF, Sevy AM, et al. (2016) Protocols for molecular modeling with Rosetta3 and RosettaScripts. *Biochemistry* **55**:4748–4763.
- Berka K, Hanák O, Sehnal D, Banás P, Navrátilová V, Jaiswal D, Ionescu CM, Svobodová Vareková R, Koca J, and Otyepka M (2012) MOLEonline 2.0: interactive web-based analysis of biomacromolecular channels. *Nucleic Acids Res* **40**(Web Server issue):W222–W227.
- Best RB, Zhu X, Shim J, Lopes PE, Mittal J, Feig M, and Mackerell AD Jr (2012) Optimization of the additive CHARMM all-atom protein force field targeting improved sampling of the backbone phi, psi and side-chain chi(1) and chi(2) dihedral angles. *J Chem Theory Comput* **8**(9):3257–3273.
- Blokhina SV, Sharapova AV, Ol'khovich MV, Volkova TV, and Perlovich GL (2016) Solubility, lipophilicity and membrane permeability of some fluoroquinolone antimicrobials. *Eur J Pharm Sci* **93**:29–37.
- Brooks BR, Brooks CL III, Mackerell AD Jr, Nilsson L, Petrella RJ, Roux B, Won Y, Archontis G, Bartels C, Boresch S, et al. (2009) CHARMM: the biomolecular simulation program. *J Comput Chem* **30**:1545–1614.
- Chen J, Seeborn G, and Sanguinetti MC (2002) Position of aromatic residues in the S6 domain, not inactivation, dictates cisapride sensitivity of HERG and eag potassium channels. *Proc Natl Acad Sci USA* **99**:12461–12466.
- Chiamvimonvat N, Chen-Izu Y, Clancy CE, Deschenes I, Dobrev D, Heijman J, Izu L, Qu Z, Ripplinger CM, Vandenberg JJ, et al. (2017) Potassium currents in the heart: functional roles in repolarization, arrhythmia and therapeutics. *J Physiol* **595**:2229–2252.
- Compton SJ, Lux RL, Ramsey MR, Strellich KR, Sanguinetti MC, Green LS, Keating MT, and Mason JW (1996) Genetically defined therapy of inherited long-QT syndrome. Correction of abnormal repolarization by potassium. *Circulation* **94**:1018–1022.
- DeMarco KR, Bekker S, Clancy CE, Noskov SY, and Vorobyov I (2018) Digging into lipid membrane permeation for cardiac ion channel blocker d-sotalol with all-atom simulations. *Front Pharmacol* **9**:26.
- Dickson CJ, Hornak V, Bednarczyk D, and Duca JS (2019) Using membrane partitioning simulations to predict permeability of forty-nine drug-like molecules. *J Chem Inf Model* **59**:236–244.
- Di Veroli GY, Davies MR, Zhang H, Abi-Gerges N, and Boyett MR (2013a) High-throughput screening of drug-binding dynamics to HERG improves early drug safety assessment. *Am J Physiol Heart Circ Physiol* **304**:H104–H117.
- Di Veroli GY, Davies MR, Zhang H, Abi-Gerges N, and Boyett MR (2013b) hERG inhibitors with similar potency but different binding kinetics do not pose the same proarrhythmic risk: implications for drug safety assessment. *J Cardiovasc Electrophysiol* **25**:197–207.
- Duff HJ, Feng ZP, and Sheldon RS (1995) High- and low-affinity sites for [3H]dofetilide binding to Guinea pig myocytes. *Circ Res* **77**:718–725.
- Ficker E, Jarolimek W, Kiehn J, Baumann A, and Brown AM (1998) Molecular determinants of dofetilide block of HERG K⁺ channels. *Circ Res* **82**:386–395.

- Friesner RA, Murphy RB, Repasky MP, Frye LL, Greenwood JR, Halgren TA, Sanschagrin PC, and Mainz DT (2006) Extra precision glide: docking and scoring incorporating a model of hydrophobic enclosure for protein-ligand complexes. *J Med Chem* **49**:6177–6196.
- Frommeyer G, Weller J, Ellermann C, Kaese S, Kochhäuser S, Lange PS, Dechering DG, and Eckardt L (2017) Antiarrhythmic properties of ivabradine in an experimental model of Short-QT- Syndrome. *Clin Exp Pharmacol Physiol* **44**:941–945.
- Gordon SE and Zagotta WN (1995) Localization of regions affecting an allosteric transition in cyclic nucleotide-activated channels. *Neuron* **14**:857–864.
- Guo J, Zhan S, Lees-Miller JP, Teng G, and Duff HJ (2005) Exaggerated block of hERG (KCNH2) and prolongation of action potential duration by erythromycin at temperatures between 37 degrees C and 42 degrees C. *Heart Rhythm* **2**:860–866.
- Gustina AS and Trudeau MC (2009) A recombinant N-terminal domain fully restores deactivation gating in N-truncated and long QT syndrome mutant hERG potassium channels. *Proc Natl Acad Sci USA* **106**:13082–13087.
- Halgren TA (2009) Identifying and characterizing binding sites and assessing druggability. *J Chem Inf Model* **49**:377–389.
- Hancox JC, Melgari D, Dempsey CE, Brack KE, Mitcheson J, and Ng GA (2015) hERG potassium channel inhibition by ivabradine may contribute to QT prolongation and risk of torsades de pointes. *Ther Adv Drug Saf* **6**:177–179.
- Harder E, Damm W, Maple J, Wu C, Reboul M, Xiang JY, Wang L, Lupyan D, Dahlgren MK, Knight JL, et al. (2016) OPLS3: a force field providing broad coverage of drug-like small molecules and proteins. *J Chem Theory Comput* **12**:281–296.
- Herzberg IM, Trudeau MC, and Robertson GA (1998) Transfer of rapid inactivation and sensitivity to the class III antiarrhythmic drug E-4031 from HERG to M-eag channels. *J Physiol* **511**:3–14.
- Hill AP, Perrin MJ, Heide J, Campbell TJ, Mann SA, and Vandenberg JI (2014) Kinetics of drug interaction with the Kv11.1 potassium channel. *Mol Pharmacol* **85**:769–776.
- Huang FD, Chen J, Lin M, Keating MT, and Sanguinetti MC (2001) Long-QT syndrome-associated missense mutations in the pore helix of the HERG potassium channel. *Circulation* **104**:1071–1075.
- Huang J, Rauscher S, Nawrocki G, Ran T, Feig M, de Groot BL, Grubmüller H, and MacKerell AD Jr (2017) CHARMM36m: an improved force field for folded and intrinsically disordered proteins. *Nat Methods* **14**:71–73.
- Jo S, Kim T, Iyer VG, and Im W (2008) CHARMM-GUI: a web-based graphical user interface for CHARMM. *J Comput Chem* **29**(11):1859–1865.
- Jorgensen WL, Chandrasekhar J, Madura JD, Impey RW, and Klein ML (1983) Comparison of Simple Potential Functions for Simulating Liquid Water. *Journal of Chemical Physics* **79**(2):926–935.
- Klauda JB, Venable RM, Freites JA, O'Connor JW, Tobias DJ, Mondragon-Ramirez C, Vorobyov I, MacKerell AD, and Pastor RW (2010) Update of the CHARMM all-atom additive force field for lipids: validation on six lipid types. *J Phys Chem* **114**(23):7830–7843.
- Kopp J and Schwede T (2004) The SWISS-MODEL Repository of annotated three-dimensional protein structure homology models. *Nucleic Acids Res* **32**:D230–234.
- Lees-Miller JP, Duan Y, Teng GQ, and Duff HJ (2000) Molecular determinant of high-affinity dofetilide binding to HERG1 expressed in *Xenopus* oocytes: involvement of S6 sites. *Mol Pharmacol* **57**:367–374.
- Lees-Miller JP, Guo J, Wang Y, Perissinotti LL, Noskov SY, and Duff HJ (2015) Ivabradine prolongs phase 3 of cardiac repolarization and blocks the HERG1 (KCNH2) current over a concentration-range overlapping with that required to block HCN4. *J Mol Cell Cardiol* **85**:71–78.
- MacKerell AD, Bashford D, Bellott M, Dunbrack RL, Evanseck JD, Field MJ, Fischer S, Gao J, Guo H, Ha S, et al. (1998) All-atom empirical potential for molecular modeling and dynamics studies of proteins. *Journal of Physical Chemistry B* **102**(18):3586–3616.
- Martyna GJ, Tobias DJ, and Klein ML (1994) Constant-pressure molecular-dynamics algorithms. *J Chem Phys* **101**:4177–4189.
- Melgari D, Brack KE, Zhang C, Zhang Y, El Harchi A, Mitcheson JS, Dempsey CE, Ng GA, and Hancox JC (2015) hERG potassium channel blockade by the HCN channel inhibitor bradycardic agent ivabradine. *J Am Heart Assoc* **4**.
- Mitcheson JS, Chen J, Lin M, Culbertson C, and Sanguinetti MC (2000) A structural basis for drug-induced long QT syndrome. *Proc Natl Acad Sci USA* **97**:12329–12333.
- Nerbonne JM and Kass RS (2005) Molecular physiology of cardiac repolarization. *Physiol Rev* **85**:1205–1253.
- Noskov SY, Berneche S, and Roux B (2004) Control of ion selectivity in potassium channels by electrostatic and dynamic properties of carbonyl ligands. *Nature* **431**(7010):830–834.
- Noskov SY and Roux B (2008) Control of ion selectivity in LeuT: Two Na⁺ binding sites with two different mechanisms. *Journal of Molecular Biology* **377**(3):804–818.
- Numaguchi H, Mullins FM, Johnson JP Jr, Johns DC, Po SS, Yang IC, Tomaselli GF, and Balser JR (2000) Probing the interaction between inactivation gating and Dd-sotalol block of HERG. *Circ Res* **87**:1012–1018.
- Perissinotti LL, De Biase PM, Guo J, Yang PC, Lee MC, Clancy CE, Duff HJ, and Noskov SY (2018) Determinants of isoform-specific gating kinetics of HERG1 channel: combined experimental and simulation study. *Front Physiol* **9**:207.
- Perlovich GL, Volkova TV, and Bauer-Brandl A (2006) Towards an understanding of the molecular mechanism of solvation of drug molecules: a thermodynamic approach by crystal lattice energy, sublimation, and solubility exemplified by paracetamol, acetanilide, and phenacetin. *J Pharm Sci* **95**:2158–2169.
- Perlovich GL and Bauer-Brandl A (2003) Thermodynamics of solutions I: benzoic acid and acetylsalicylic acid as models for drug substances and the prediction of solubility. *Pharm Res* **20**:471–478.
- Perry M, Sachse FB, and Sanguinetti MC (2007) Structural basis of action for a human ether-a-go-go-related gene 1 potassium channel activator. *Proc Natl Acad Sci USA* **104**:13827–13832.
- Perry M, Sanguinetti M, and Mitcheson J (2010) Revealing the structural basis of action of hERG potassium channel activators and blockers. *J Physiol* **588**:3157–3167.
- Phillips JC, Braun R, Wang W, Gumbart J, Tajkhorshid E, Villa E, Chipot C, Skeel RD, Kalé L, and Schulten K (2005) Scalable molecular dynamics with NAMD. *J Comput Chem* **26**(16):1781–1802.
- Roden DM, Lazzara R, Rosen M, Schwartz PJ, Towbin J, and Vincent GM (1996) Multiple mechanisms in the long-QT syndrome. Current knowledge, gaps, and future directions. The SADS Foundation Task Force on LQTS. *Circulation* **94**:1996–2012.
- Sale H, Wang J, O'Hara TJ, Tester DJ, Phartiyal P, He JQ, Rudy Y, Ackerman MJ, and Robertson GA (2008) Physiological properties of hERG 1a/1b heteromeric currents and a hERG 1b-specific mutation associated with Long-QT syndrome. *Circ Res* **103**:e81–e95.
- Sanguinetti MC (2014) HERG1 channel agonists and cardiac arrhythmia. *Curr Opin Pharmacol* **15**:22–27.
- Sanguinetti MC, Jiang C, Curran ME, and Keating MT (1995) A mechanistic link between an inherited and an acquired cardiac arrhythmia: HERG encodes the IKr potassium channel. *Cell* **81**:299–307.
- Saxena P, Zangerl-Plessl EM, Linder T, Windisch A, Hohaus A, Timin E, Hering S, and Stary-Weinzinger A (2016) New potential binding determinant for hERG channel inhibitors. *Sci Rep* **6**:24182.
- Schönherr R and Heinemann SH (1996) Molecular determinants for activation and inactivation of HERG, a human inward rectifier potassium channel. *J Physiol* **493**:635–642.
- Schrödinger LLC (2016) *Schrödinger Suite 2018-2 Induced Fit Docking Protocol*, Glide, Schrodinger LLC, New York.
- Shan Y, Klepeis JL, Eastwood MP, Dror RO, and Shaw DE (2005) Gaussian split Ewald: a fast Ewald mesh method for molecular simulation. *J Chem Phys* **122**:54101.
- Shaw DE, Grossman JP, Bank JA, Batson B, Butts JA, Chao JC, Deneroff MM, Dror RO, Even A, Fenton CH, et al. (2014) Anton 2: raising the bar for performance and programmability in a special-purpose molecular dynamics supercomputer, in *SC14: Proceedings of the International Conference for High Performance Computing, Networking, Storage and Analysis*, 41–53, IEEE Press, Piscataway, NJ.
- Shoichet BK and Kobilka BK (2012) Structure-based drug screening for G-protein-coupled receptors. *Trends Pharmacol Sci* **33**:268–272.
- Spector PS, Curran ME, Zou A, Keating MT, and Sanguinetti MC (1996) Fast inactivation causes rectification of the IKr channel. *J Gen Physiol* **107**:611–619.
- Splawski I, Tristani-Firouzi M, Lehmann MH, Sanguinetti MC, and Keating MT (1997) Mutations in the hminK gene cause long QT syndrome and suppress IKs function. *Nat Genet* **17**:338–340.
- Stork D, Timin EN, Berjukow S, Huber C, Hohaus A, Auer M, and Hering S (2007) State dependent dissociation of HERG channel inhibitors. *Br J Pharmacol* **151**:1368–1376.
- Thompson JD, Higgins DG, and Gibson TJ (1994) CLUSTAL W: improving the sensitivity of progressive multiple sequence alignment through sequence weighting, position-specific gap penalties and weight matrix choice. *Nucleic Acids Res* **22**(22):4673–4680.
- Trudeau MC, Warmke JW, Ganetzky B, and Robertson GA (1995) HERG, a human inward rectifier in the voltage-gated potassium channel family. *Science* **269**:92–95.
- Vandenberg JI, Perozo E, and Allen TW (2017) Towards a structural view of drug binding to hERG K⁺ channels. *Trends Pharmacol Sci* **38**:899–907.
- Vandenberg JI, Perry MD, Perrin MJ, Mann SA, Ke Y, and Hill AP (2012) hERG K⁺ channels: structure, function, and clinical significance. *Physiol Rev* **92**:1393–1478.
- Vandenberg JI, Walker BD, and Campbell TJ (2001) HERG K⁺ channels: friend and foe. *Trends Pharmacol Sci* **22**:240–246.
- Vasilef I (2013) *Data Analysis and Scientific Visualization*, Universiteit Utrecht, Utrecht, Netherlands.
- Wacker S and Noskov SY (2018) Performance of machine learning algorithms for qualitative and quantitative prediction drug blockade of hERG1 channel. *Comput Toxicol* **6**:55–63.
- Wacker S, Noskov SY, and Perissinotti LL (2017) Computational models for understanding of structure, function and pharmacology of the cardiac potassium channel Kv11.1 (hERG). *Curr Top Med Chem* **17**:2681–2702.
- Wang W and MacKinnon R (2017) Cryo-EM structure of the open human ether-a-go-go-related K⁺ channel hERG. *Cell* **169**:422–430.e10.
- Wang Y, Guo J, Perissinotti LL, Lees-Miller J, Teng G, Durdagi S, Duff HJ, and Noskov SY (2016) Role of the pH in state-dependent blockade of hERG currents. *Sci Rep* **6**:32536.
- Whicher JR and MacKinnon R (2016) Structure of the voltage-gated K⁺ channel Eag1 reveals an alternative voltage sensing mechanism. *Science* **353**:664–669.
- Witchel HJ (2011) Drug-induced hERG block and long QT syndrome. *Cardiovasc Ther* **29**:251–259.
- Wu W, Gardner A, and Sanguinetti MC (2014) Cooperative subunit interactions mediate fast C-type inactivation of hERG1 K⁺ channels. *J Physiol* **592**:4465–4480.
- Wu W, Gardner A, and Sanguinetti MC (2015) The link between inactivation and high-affinity block of hERG1 channels. *Mol Pharmacol* **87**:1042–1050.
- Zhao C, Caplan DA, and Noskov SY (2010) Evaluations of the absolute and relative free energies for antidepressant binding to the amino acid membrane transporter LeuT with free energy simulations. *J Chem Theory Comput* **6**:1900–1914.

Address correspondence to: Dr. Henry J. Duff, Cumming School of Medicine, Libin Institute, University of Calgary, HRC GC73, 3280 Hospital Drive NW, Calgary, Alberta, Canada T2N 4Z6. E-mail: hduff@ucalgary.ca; or Dr. Sergei Yu Noskov, Department of Biological Sciences, University of Calgary, 2500 University Drive, Alberta, Canada, T2N 1N4. E-mail: snoskov@ucalgary.ca

SUPPLEMENTARY MATERIALS

The Pore-Lipid interface: Role of Amino Acid Determinants of Lipophilic Access by Ivabradine to the hERG1Pore Domain

Laura Perissinotti,^{1†} Jiqing Guo,^{2†} Meruyert Kudaibergenova,^{1†} James Lees-Miller², Marina Ol'khovich³, Angelica Sharapova³, German L. Perlovich³, Daniel A Muruve⁴, Brenda Gerull⁵, Sergei Yu. Noskov^{1*} and Henry J. Duff^{2*}

Summary: Electrophysiology data on the impact of mutations on inactivation process with and without ivabradine, Specific Protocols for Ivabradine and Dofetilide partitioning experiments, Summary of molecular docking and additional MD analysis.

Experimental Protocols for Drug Partitioning Experiments

Materials

Dofetilide (CAS No. 115256-11-6) and Ivabradine hydrochloride (CAS No. 148849-67-6) were purchased with 99.4 % purity declared by the providers. The drug quality was controlled with DSC measurements as reported previously (Karimi-Jafari et al., 2018; Perlovich et al., 2004; Perlovich et al., 2006). n-Hexane (CAS No. 110-54-3) was purchased from Sigma-Aldrich with declared purity ≥ 97 %. Bi-distilled water (with electrical conductivity $2.1 \mu\text{S cm}^{-1}$) was used to prepare buffer solutions. Phosphate buffer pH 7.4 ($I=0.15 \text{ mol/l}$) was prepared by combining KHPO_4 (9.1 g in 1 l) and $\text{NaH}_2\text{PO}_4 \cdot 12\text{H}_2\text{O}$ (23.6 g in 1 l) salts. The pH values were measured by using a pH meter FG2-Kit (Mettler Toledo, Switzerland) standardized with pH 1.68, 6.86 and 9.22 solutions.

Differential scanning calorimetry

Melting temperature of the compound studied has been determined using a Perkin-Elmer Pyris 1 DSC differential scanning calorimeter (Perkin-Elmer Analytical Instruments, Norwalk, Connecticut, USA) with Pyris software for Windows NT. DSC runs were performed in an atmosphere of flowing $20 \text{ cm}^3 \cdot \text{min}^{-1}$ dry helium gas of high purity 0.99996 (mass fraction) using standard aluminum sample pans and a heating rate of $2 \text{ K} \cdot \text{min}^{-1}$. The accuracy of weight measurements was 0.05 mg. The DSC was calibrated using a two-point calibration, measuring the onset melting temperatures of indium and zinc standards as onset melting is almost independent of the scan rate. Temperatures of melting for indium and zinc were

429.7 K and 419.5 °C, respectively (determined by at least ten measurements). The enthalpy scale was calibrated using the heat of fusion of indium. The value measured for the enthalpy of fusion corresponded to 28.69 J·g⁻¹ (reference value 28.66 J·g⁻¹). Uncertainty for melting temperature corresponds to expanded uncertainty of the mean (confidence level: 0.95). Thermal stability of drugs were studied using differential scanning calorimetry in order to establish a comparison guide for available thermodynamic data (Karimi-Jafari et al., 2018). Briefly, the DSC curve of dofetilide revealed two endothermic regions: the first one is shown by the peak with the maximum at 135.9 °C, and the second one is at 139.6 °C. The obtained data show that dofetilide of this study is a mixture of two polymorph in an agreement with previous reports that also utilized differential scanning calorimetry. The differences observed in the melting points of the polymorphs are explained by various degrees of order of these crystalline structures. All of these polymorphs are bioactive and have the same therapeutic properties thus, the drug used in medical practice is a mixture of polymorphs (Appleby et al., 1999). The thermal curve of the ivabradine hydrochloride represented a profile of the pure crystalline anhydrous compound with a sharp endothermic peak and onset melting temperature $T_m = 195.5$ °C. Maximum of peak corresponded $T_m = 200.7$ °C. The melting process is accompanied with a decomposition of the compound characterized by an exothermic peak. The obtained melting temperature for ivabradine was in agreement with the data presented in Chemical Book [<https://www.chemicalbook.com>] and in the corresponding patents for various crystalline forms of the drug (Horvath, 2005).

Supplementary Table 1: *P-values* from One-Way ANOVA analysis of Electrophysiological Experiments summarized in Figure 4

Supplementary Table 2. Detailed results of ensemble MD docking of hERG1 transmembrane (TM) open model with neutral state ivabradine to selected MD frames of WT and mutants. Poses were clustered into 3 binding sites: Cavity, Lipophilic and “access path”. Each clustered site was further subdivided by 4 different subunits (adjacent chains). The percentages of poses found within the binding for each subunit and the overall average is reported.

Supplementary Table 3. Detailed results of ensemble MD docking of hERG transmembrane (TM) open model with neutral state ivabradine to selected MD frames of WT and mutants. Poses were clustered into 3 binding sites: Cavity, Lipophilic and “access path”. Each clustered site was further subdivided by 4 different subunits (adjacent chains). The number of poses found within the binding for each subunit and the binding average energy (kcal/mol) is reported.

Supplementary Table 4 (shown together with Supplementary Figure 14): Results of the energy score of extra-precision (XP) docking of cationic forms of common hERG1 blockers to major intracavitary site with three different states of hERG1 channel mapped from the dominant clusters in all-atom MD simulation. Frequency of docking occurrences I also reported in the brackets. Only poses < 2.5 kcal/mol were accounted for.

Supplementary Figures Legends

Supplementary Figure 1. The dose-response relationship of ivabradine in each M651X mutations. The curves were fitted to Hill's equation, except for M651T & M651V which were smoothly connected. N varied from 2 to 6 for each point.

Supplementary Figure 2. Comparative analysis of IC₅₀s of ivabradine binding to selected M651X systems vs. the residue contribution to free energy of partitioning (Wimley and White, 1996) (A); octanol partitioning (B) and residue volume (C) (Zamyatnin, 1972) and Accessible Surface Area ((Chothia, 1976)

Supplementary Figure 3. IC₅₀s of ivabradine binding to selected M651X in relationship with their baseline current characteristics; activation $V_{1/2}$ (A), deactivation slow time-constant (B), inactivation $V_{0.3}$ (C) and inactivation recovery time-constant (D). Linear regression fitting was used in D. N=3 per point.

Supplementary Figure 4. IC₅₀ of ivabradine binding to selected M651X mutants and drug-induced current characteristic changes; activation $V_{1/2}$ (A), deactivation slow time-constant (B), inactivation $V_{0.3}$ (C) and inactivation recovery time-constant (D). N=3 per point for each mutation. Linear regression fitting was used for data in Panels B and D.

Supplementary Figure 5: Average backbone RMSD fluctuations for the full MD trajectory run for WT hERG1 (open) and EAG1 Model (closed), along with mutants. The cartoon representation of the protein sections is in green. Colored bars indicate the position of residues F557 (green), M651 (orange) and F656 (purple).

Supplementary Figure 6: Molecular topology for the alternative docking site: between the lipophilic and internal cavity sites. Ivabradine depicted binding to the WT hERG1 in the open state.

Supplementary Figure 7. F557 and F656 rotational dynamics and stability of the hydrophobic interactions between residues. **A)** Time evolution of selected (C_{α} - C_{β} - C_{γ} - $C_{\delta 1}$) dihedral angle for F656 (D2) and F557 (D1). **B)** Relative position of F557 and F656 in WT-hERG1 Cryo-EM structure. Dihedrals and relevant distances are shown as D1, D2 with shadowed circles and dashed lines respectively. Position of M651 is highlighted (orange) in the protein backbone.

Supplementary Figure 8. F557 and F656 rotational flexibility and their interaction from the equilibrated trajectory (last 400 ns). **A)** Time evolution of selected ($C\alpha$ - $C\beta$ - $C\gamma$ - $C\delta 1$) dihedral angle for F656 (D2) and F557 (D1) for hEAG1 (closed hERG1 Model). **B)** Time evolution of selected ($C\alpha$ - $C\beta$ - $C\gamma$ - $C\delta 1$) dihedral angle for F656 (D2) for F557L mutant. **C)** Time evolution of selected ($C\alpha$ - $C\beta$ - $C\gamma$ - $C\delta 1$) dihedral angle for F656 (D1) for M651T/F557L mutant.

Supplementary Figure 9. Side-representation of hERG1 tetramer (protomers are labeled as A, B, C and D, respectively) illustrating relevant access pathways mapped with MOLE Online tool. Topology, length and properties like hydrophobicity are shown for each access pathway. Relevant residues mutated in this work (F557, M651) combined with F656 and Y652 mutations to probe different pathways mapped in this work.

Supplementary Figure 10. Side-view of the ivabradine poses (represented by magenta stick) shown for WT, M651T, M651T/F557L and F557L hERG1 channels. The Pore Domain is shown in teal, Voltage Sensing Domain is shown in green.

Supplementary Figure 11. Zoom-in view for topology of the ivabradine binding to different sites of the Pore Domain (PD) and the Trans-Membrane Domain (TMD) of WT and mutant hERG1 (The figure is the same as Figure 5, but one of the monomer's structure is removed for clarity purposes). **Left:** Induced-Fit Docking (IFD) of ivabradine to PD access site (top left), lipophilic site (middle) and intracellular cavity site (bottom). Ivabradine is shown in magenta and relevant interacting residues are labeled. The arrows indicate the potential access route that the drug may follow to access the internal cavity and induce the block. **Center:** Ensemble of binding poses mapped from the IFD docking showing the exploration of the different binding sites for WT (top), M651T (middle) and F557LM651T (bottom) of the PD of hERG1. No poses were found in the access path site for M651T. **Right:** Group of poses found by MD-ensemble docking showing the exploration of the different binding sites for WT (top), M651T (middle) and F557LM651T (bottom) TM hERG1. Results only from one of the four subunits are

shown for clarity. Results for all subunits are displayed in the corresponding pie charts beside each system and in Table 2. In agreement with IDF docking performed with Cryo-EM structure, almost no poses were found on the access path site for the M651T mutant.

Supplementary Figure 12: Topology of the lipid-facing binding pocket. Ivabradine is shown in magenta and relevant interacting residues are labeled.

Supplementary Figure 13: Top- and side-views of the intra-cavitary binding pocket in hERG1. Ivabradine is shown in magenta and relevant interacting residues are labeled.

Supplementary Figure 14: Docking was performed on Maestro (Schrodinger) using 3 different states of the WT hERG1. Each ligand was prepared using LigPrep (sampled ring conformations and different state of the charged group corresponding to pH 7.4). Replication of the same dockings with the same receptor structure yielded identical results. **Panel A** shows various views of the docking grid. **Panel B** shows differences in F656 orientation observed in major structural states from all-atom MD simulations.

Supplementary Table 1: P-values from One-Way ANOVA analysis of Electrophysiological Experiments summarized in Figure 4

<i>Panel #</i>	<i>Cross-correlation between mutations</i>	<i>P-value</i>
A	M651T/F656C vs. M651T	<0.001
A	M651T/F656C vs. F656C	<0.001
A	F656C vs. M651T	<0.001
B	M651T/Y656A vs. Y652A	0.004
B	M651T/Y656A vs. M651T	0.003
B	Y652A vs. M651T	0.948
C	M651T/S620T vs M651T	<0.001
C	M651T/S620T vs S620T	<0.001
C	S620T vs M651T	0.65
D	M651T/F557L vs F557L	<0.001
D	M651T/F557L vs M651T	<0.001
D	F557L vs M651T	0.3
E	F656C/Y652A vs Y652A	<0.001
E	F656C/Y652A vs F656C	0.007
E	F656C vs Y652A	0.032
F	S620T/F557L vs F557L	0.068
F	S620T/F557L vs S620T	0.072
F	S620T vs F557L	0.763

Supplementary Table 2: Detailed results of ensemble MD docking of hERG1 transmembrane (TM) open model with neutral state ivabradine to selected MD frames of WT and mutants. Poses were clustered into 3 binding sites: Cavity, Lipophilic and “access path”. Each clustered site was further subdivided by 4 different subunits (adjacent chains). The percentages of poses found within the binding for each subunit and the overall average is reported.

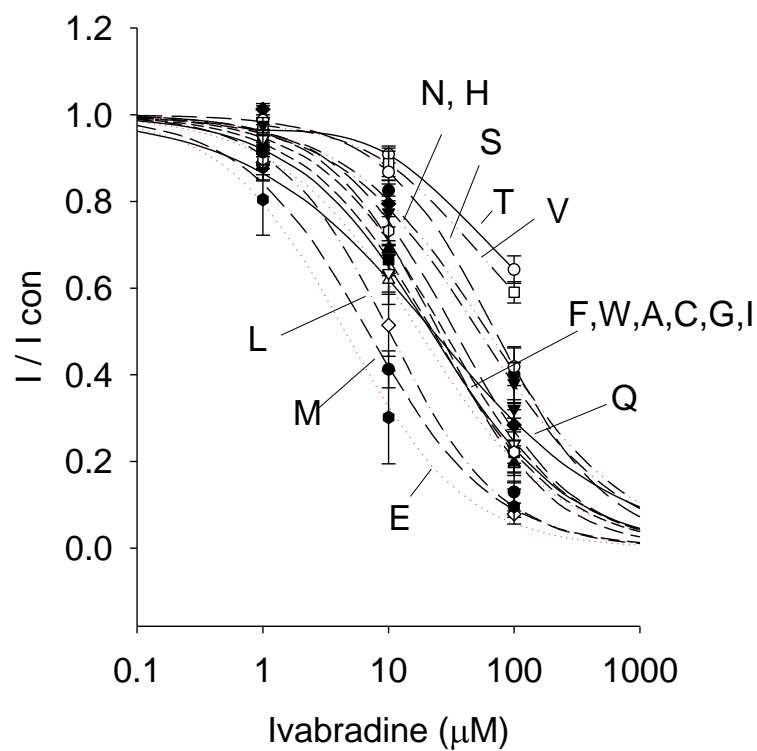
Studied system		Cavity				Lipophilic				Access Path			
		A-D	B-C	A-B	C-D	A-D	B-C	A-B	C-D	A-D	B-C	A-B	C-D
WT	Percentage of poses	12.8%	58.7%	62%	39.1%	83%	8.5%	20%	60.9%	4.2%	32.6%	18%	0%
	Average	43.2%				43.1%				13.7%			
M651T	Percentage of poses	43.1%	100%	64.6%	80.9%	54.9%	0%	31.3%	14.9%	2%	0%	4.2%	4.2%
	Average	72.1%				25.3%				2.6%			
F557L	Percentage of poses	71%	100%	9.3%	88.2%	28.6%	0%	72.1%	5.9%	0%	0%	18.6%	5.9%
	Average	67.2%				26.6%				6.1%			
F557L/M651T	Percentage of poses	41.7%	43.9%	21.1%	60.4%	14.6%	41.5%	34.2%	18.9%	43.7%	14.6%	44.7%	20.7%
	Average	41.8%				27.3%				30.9%			

Supplementary Table 3: Detailed results of ensemble MD docking of hERG1 transmembrane (TM) open model with neutral state ivabradine to selected MD frames of WT and mutants. Poses were clustered into 3 binding sites: Cavity, Lipophilic and “access path”. Each clustered site was further subdivided by 4 different subunits (adjacent chains). The number of poses found within the binding for each subunit and the binding average energy (kcal/mol) is reported.

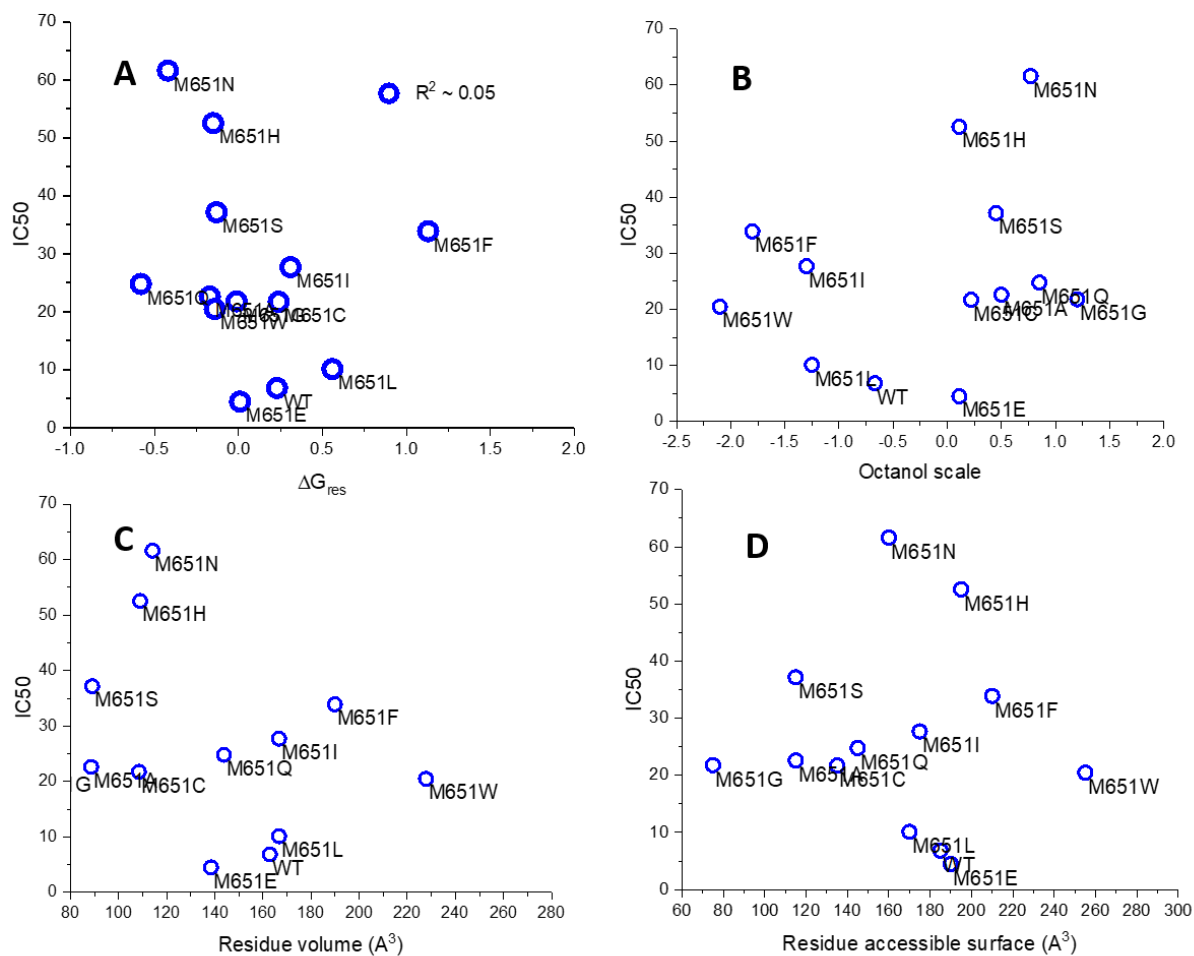
System/Binding sites	Cavity (kcal/mol)					Lipophilic (kcal/mol)					In-between (kcal/mol)				
	Adjacent Chains				Total	Number of Poses (#)				Total	Adjacent Chains				Total
	A-D	B-C	A-B	C-D		A-D	B-C	A-B	C-D		A-D	B-C	A-B	C-D	
	A-D	B-C	A-B	C-D		A-D	B-C	A-B	C-D		A-D	B-C	A-B	C-D	
WT	6	27	31	9	73	39	4	10	14	67	2	15	9	0	27
M651T	22	53	31	38	144	28	0	15	7	50	1	0	2	2	5
F557L	15	43	4	45	107	6	0	31	3	40	4*	0	4	3	11
F557L/M651T	20	18	8	32	78	7	17	13	10	47	21	6	17	11	55

	Binding Energy (kcal/mol)					Binding Energy (kcal/mol)					Binding Energy (kcal/mol)				
	Adjacent Chains				Total	Adjacent Chains				Total	Adjacent Chains				Total
	A-D	B-C	A-B	C-D		A-D	B-C	A-B	C-D		A-D	B-C	A-B	C-D	
	A-D	B-C	A-B	C-D		A-D	B-C	A-B	C-D		A-D	B-C	A-B	C-D	
WT	-4.39 ± 0.55	-5.32 ± 1.50	-5.20 ± 1.63	-5.71 ± 0.93	-5.22 ± 1.45	-5.08 ± 0.91	-3.90 ± 0.36	-4.57 ± 0.71	-4.19 ± 0.85	-4.72 ± 0.93	-3.97 ± 0.52	-4.14 ± 0.97	-4.72 ± 0.63	0.00	-4.42 ± 0.93
M651T	-5.26 ± 1.33	-6.06 ± 1.23	-5.75 ± 1.26	-5.43 ± 1.37	-5.71 ± 1.31	-4.58 ± 0.72	0.00	-4.53 ± 0.68	-4.73 ± 1.08	-4.58 ± 0.74	-3.76	0.00	-5.20 ± 2.08	-3.39 ± 0.22	-4.19 ± 1.40
F557L	-4.72 ± 0.93	-6.10 ± 1.19	-4.09 ± 0.37	-5.47 ± 1.24	-5.57 ± 1.27	-3.5 ± 0.26	0.00	-5.02 ± 0.79	-4.43 ± 0.19	-4.75 ± 0.89	-4.21 ± 0.86	0.00	-4.57 ± 0.62	-4.00 ± 0.63	-4.27 ± 0.72
F557L/M651T	-5.40 ± 1.35	-4.79 ± 1.02	-5.24 ± 1.35	-4.81 ± 0.77	-4.69 ± 1.10	-5.40 ± 1.35	-5.02 ± 0.52	-4.58 ± 1.60	-4.52 ± 0.51	-4.76 ± 0.99	-4.35 ± 0.84	-4.67 ± 1.44	-5.04 ± 1.35	-4.82 ± 0.83	-5.00 ± 1.08

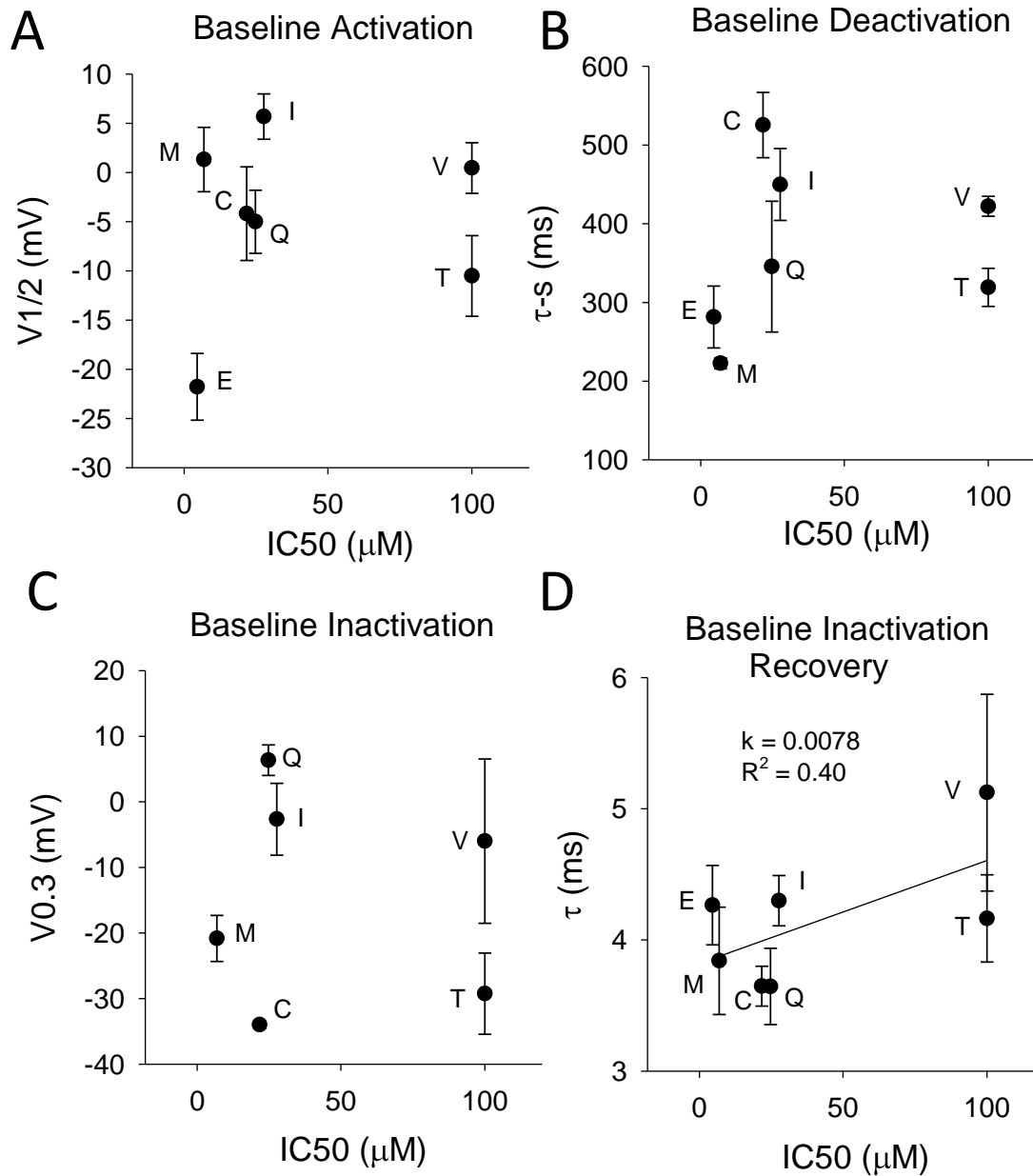
Supplementary Figure 1: The dose-response relationship of Ivabradine in each M651X mutations. The curves were fitted to Hill's equation, except M651T & M651V which were just connected smoothly. N=2 – 6 for each points.



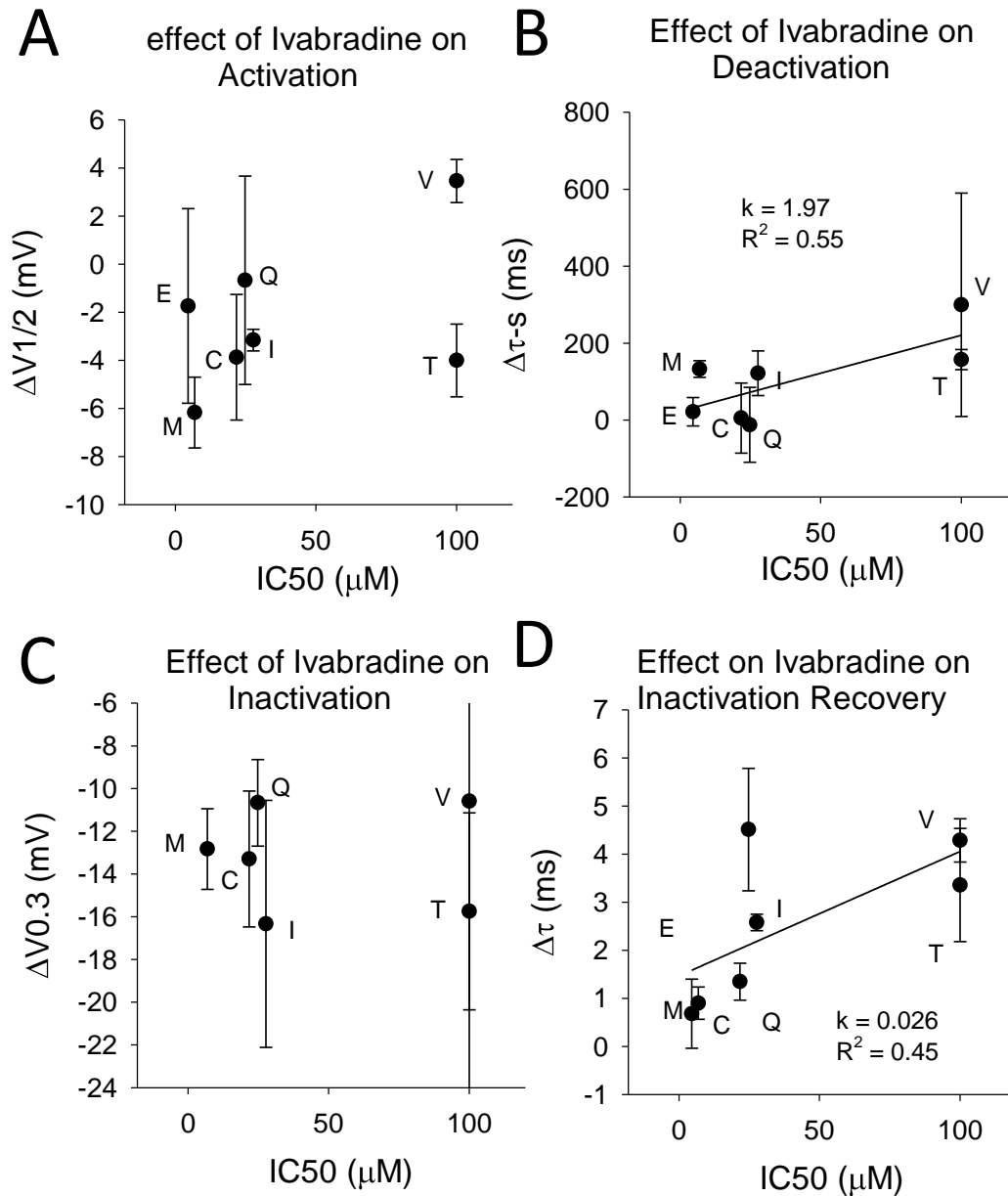
Supplementary Figure 2 Comparative analysis of IC50s of ivabradine binding of selected M651X systems vs. Whole residue contribution to free energy of partitioning(Wimley and White, 1996) (A); octanol partitioning (B); residue volume (C)(Zamyatnin, 1972) and Accessible Surface Area ((Chothia, 1976)



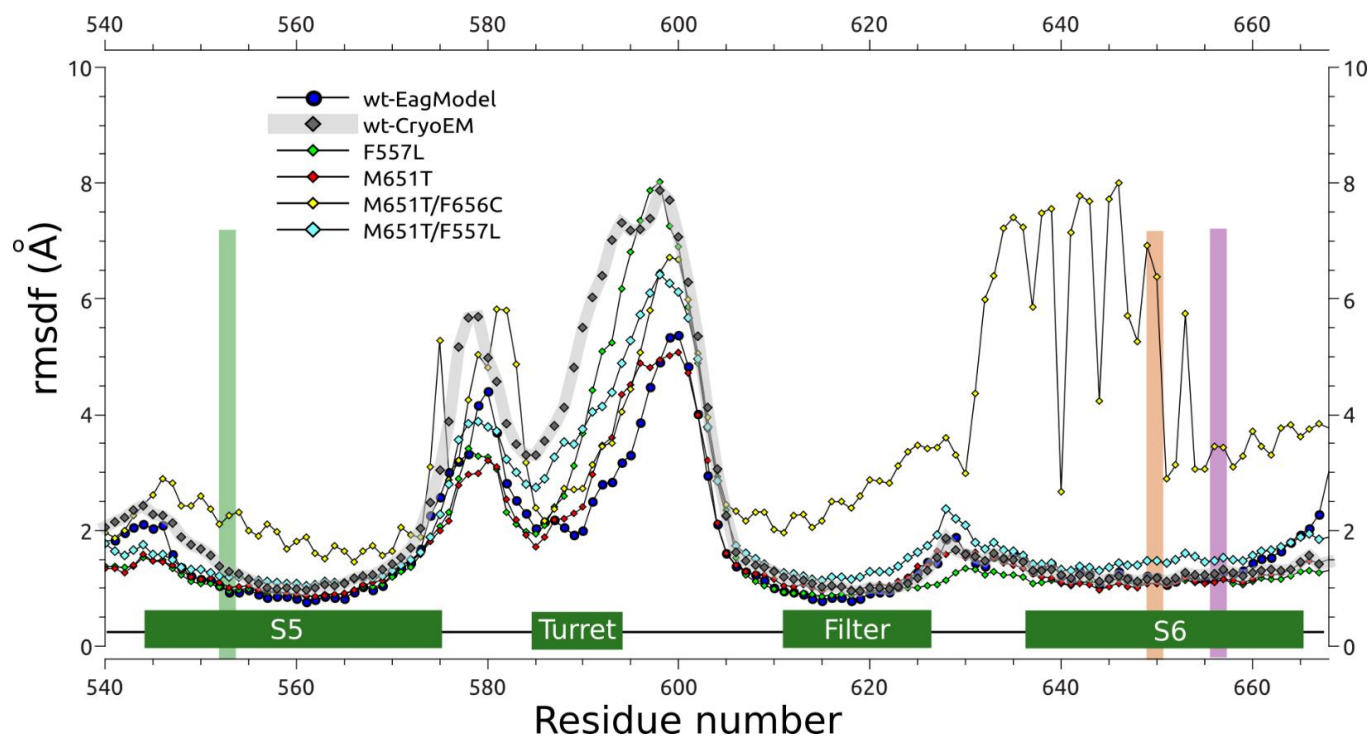
Supplementary Figure 3. Ivabradine IC50s of M651X in relationship with their baseline current characteristics; activation V1/2 (A), deactivation slow time-constant (B), inactivation V0.3 (C) and inactivation recovery time-constant (D). Linear regression fitting was used in D. N=3 per point.



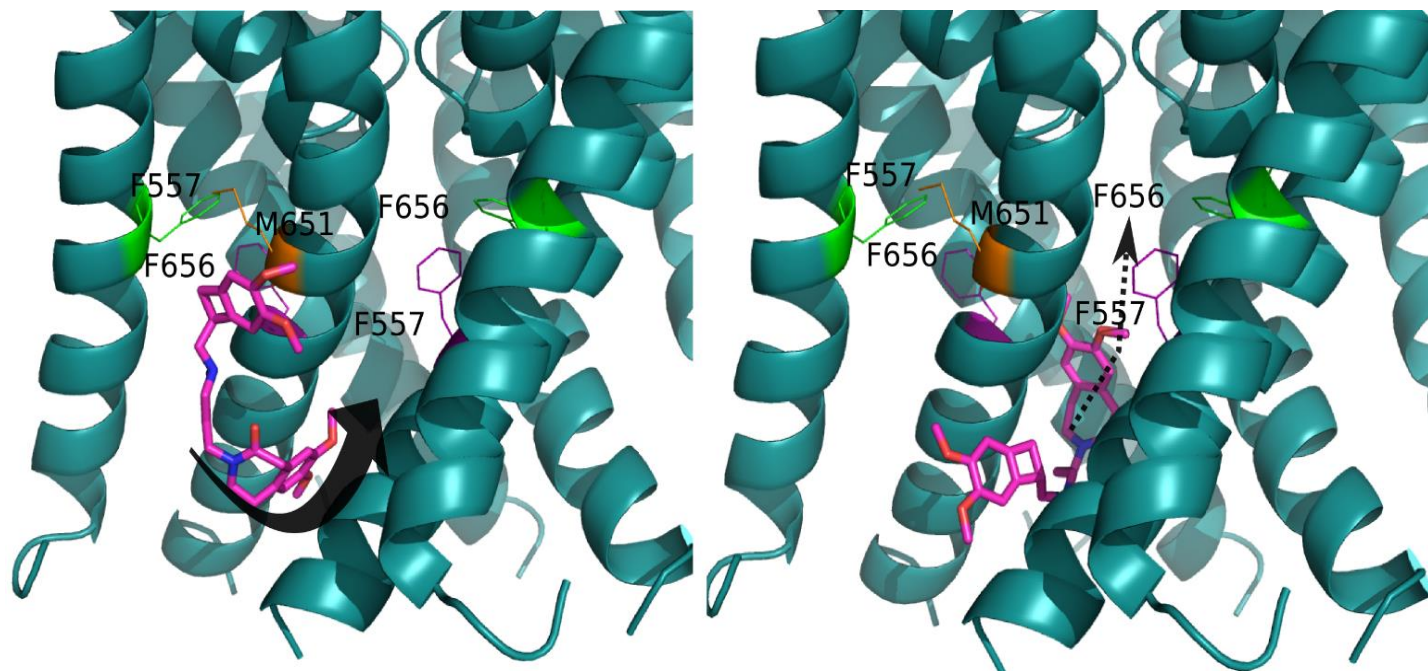
Supplementary Figure 4. Ivabradine IC₅₀s of M651X in relationship with their baseline current characteristics; activation V_{1/2} (A), deactivation slow time-constant (B), inactivation V_{0.3} (C) and inactivation recovery time-constant (D). Linear regression fitting was used in the panel D. N= 3 per point.



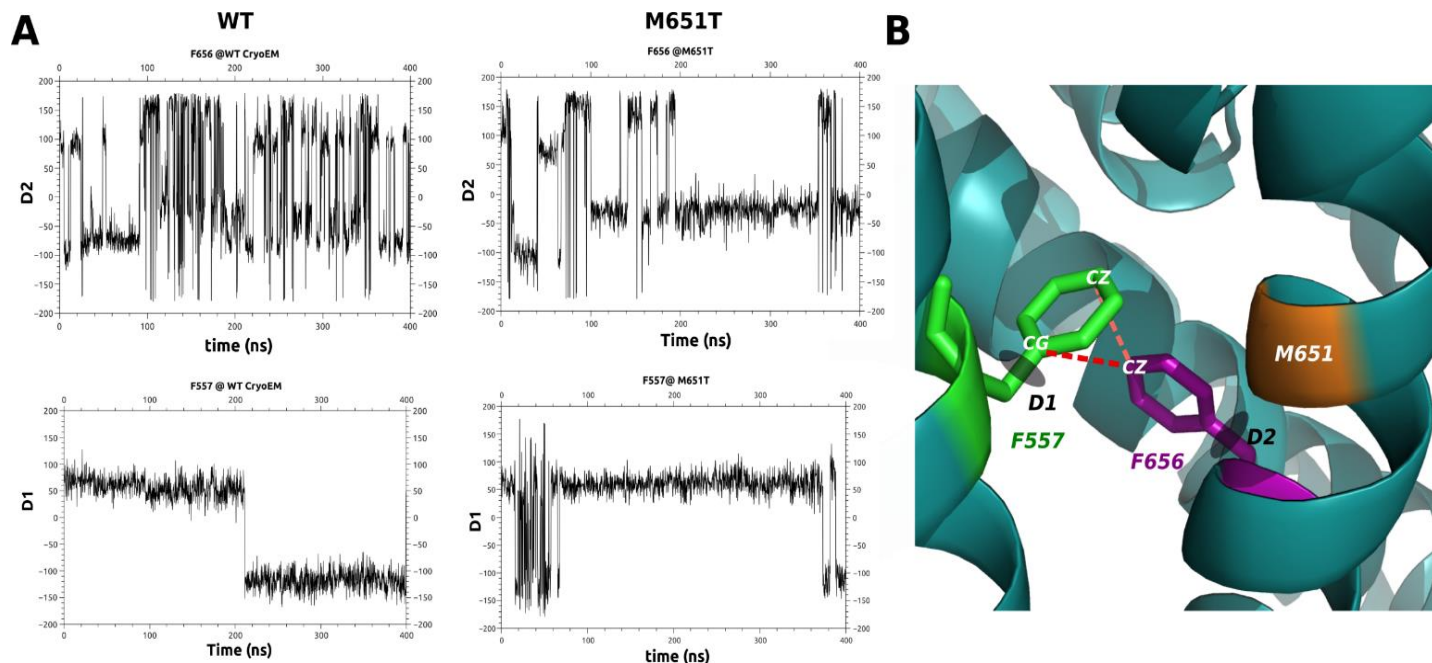
Supplementary Figure 5: Average backbone RMSD fluctuations from the full MD trajectory run for the WT hERG1 (open state), hEAG1 Model (closed state), and mutants. Cartoon representation of the protein sections is depicted in green. Colored bars indicate the position of residues F557 (green), M651 (orange) and F656 (purple).



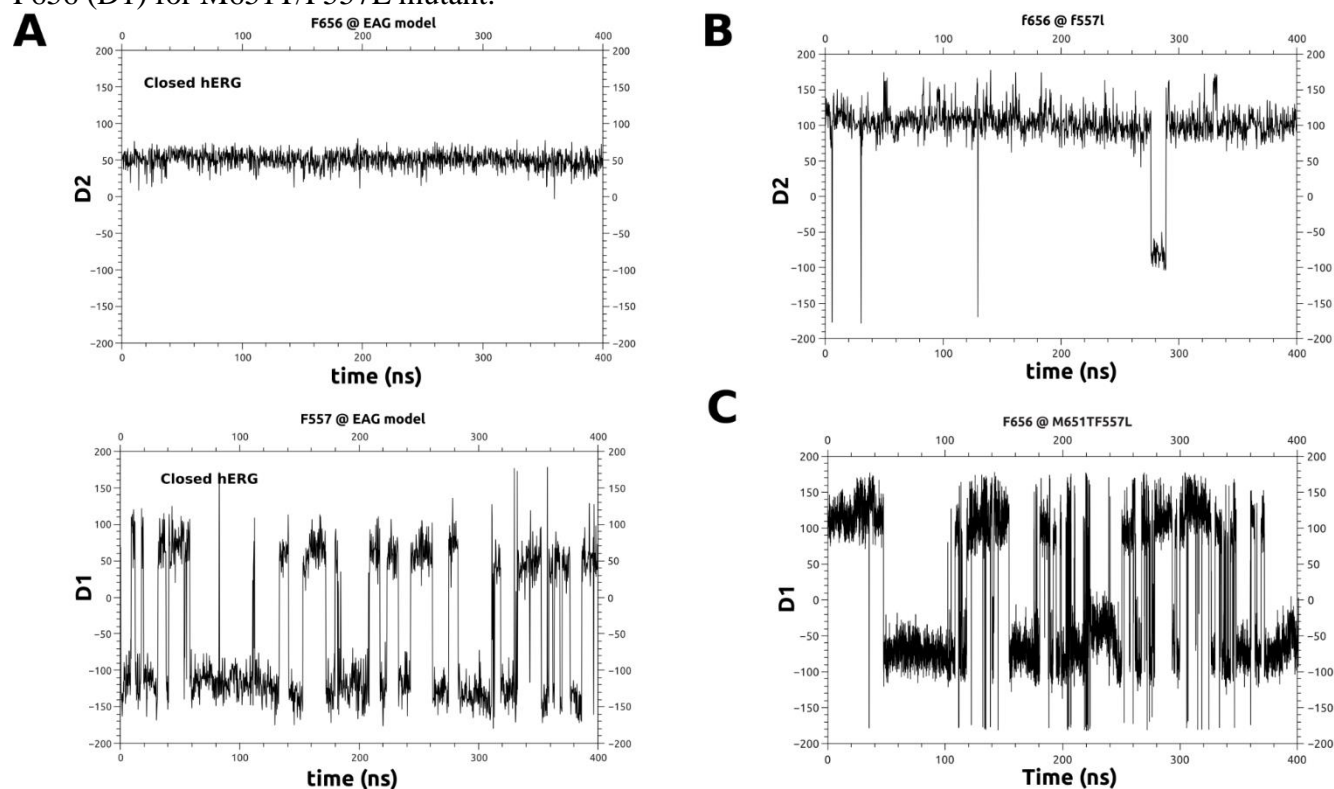
Supplementary Figure 6: Alternative docking site: between the lipophilic and the internal cavity site. Ivabradine is depicted binding to the WT hERG1 (open state).



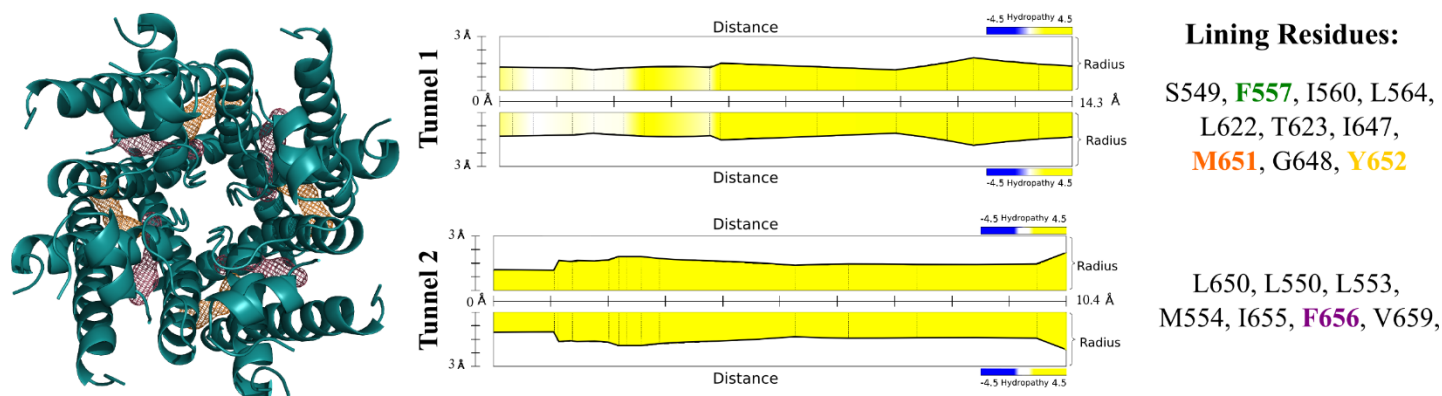
Supplementary Figure 7. F557 and F656 rotational dynamics and stability of hydrophobic interactions. **A)** Time evolution of selected (C_{α} - C_{β} - C_{γ} - $C_{\delta 1}$) dihedral angle for F656 (D2) and F557 (D1). **B)** Relative position of F557 and F656 of WThERG1 Cryo EM structure. Dihedrals and relevant distances are shown as D1, D2 with shadowed circles and dashed lines respectively. Position of M651 is highlighted (orange) in the protein backbone.



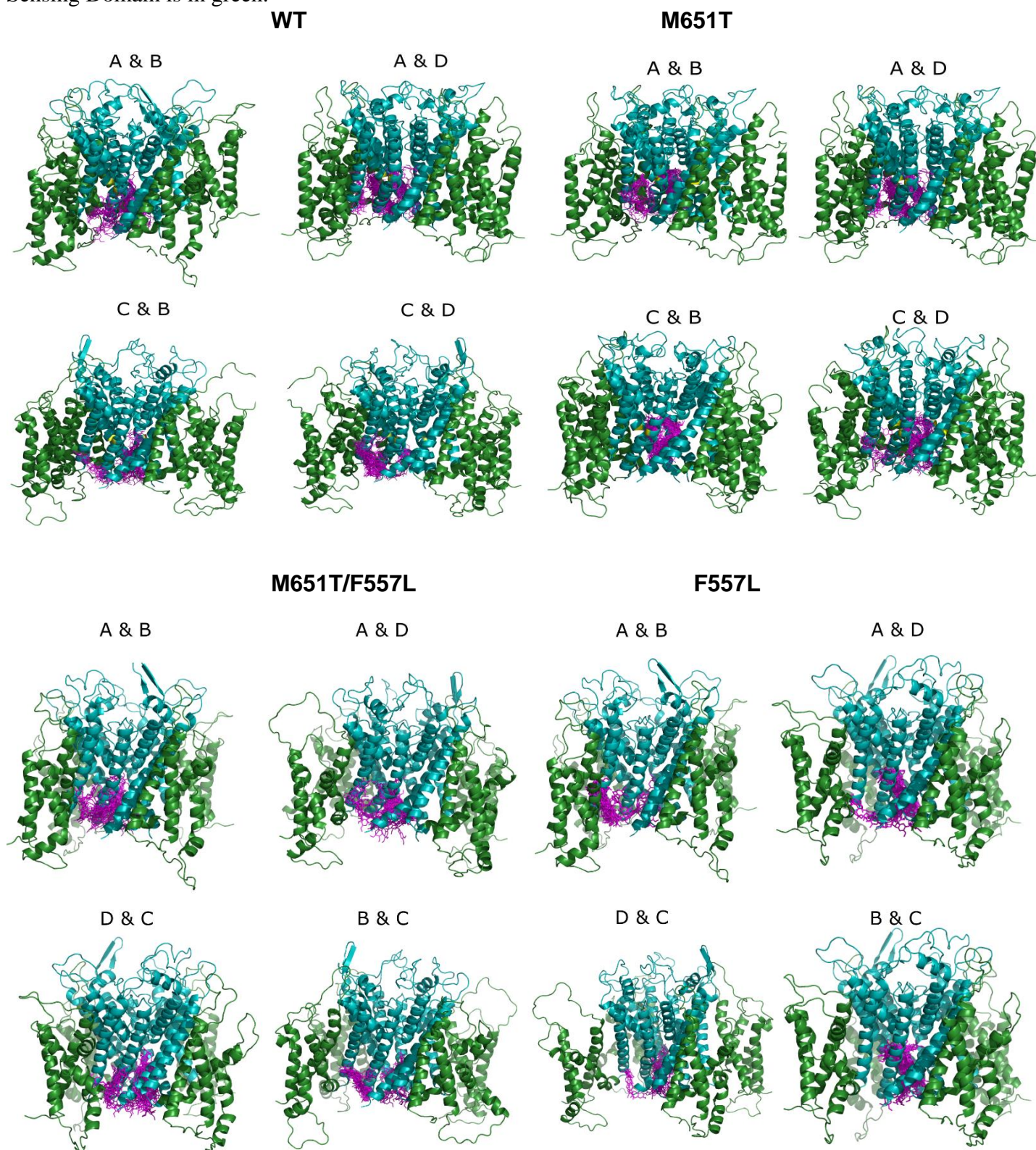
Supplementary Figure 8. F557 and F656 rotational flexibility and interactions from equilibrated trajectory (last 400 ns). **A)** Time evolution of selected (C_{α} - C_{β} - C_{γ} - $C_{\delta 1}$) dihedral angle for F656 (D2) and F557 (D1) for the hEAG closed hERG1 Model. **B)** Time evolution of selected (C_{α} - C_{β} - C_{γ} - $C_{\delta 1}$) dihedral angle for F656 (D2) for F557L mutant. **C)** Time evolution of selected (C_{α} - C_{β} - C_{γ} - $C_{\delta 1}$) dihedral angle for F656 (D1) for M651T/F557L mutant.



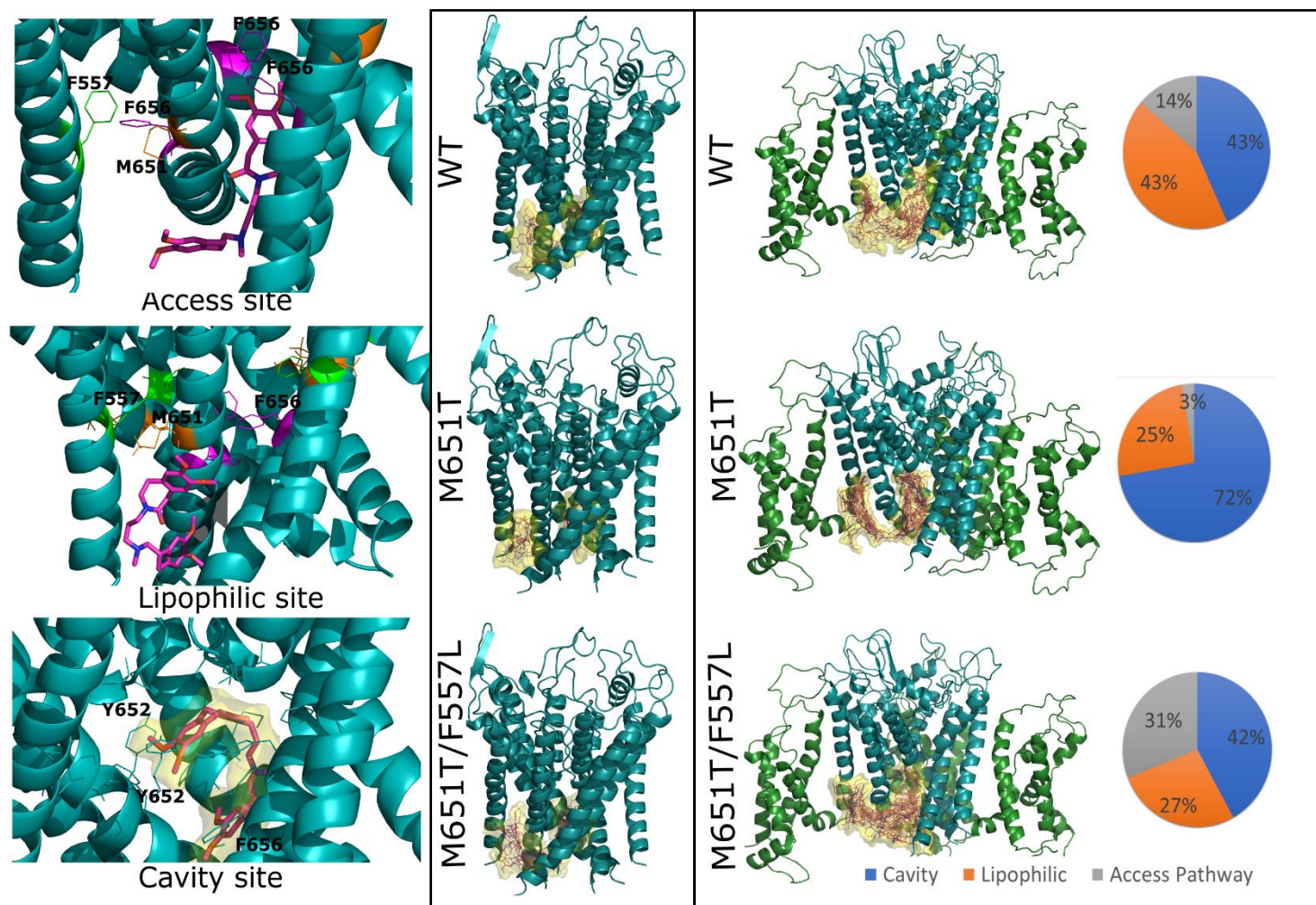
Supplementary Figure 9. Side-views of hERG1 tetramer (protomers are labeled as A, B, C and D, respectively) illustrating relevant access pathways mapped with MOLE Online tool. Topology, length and properties like hydrophobicity are shown for each access pathway. Relevant residues mutated in this work (F557, M651) together with other key ones like F656 and Y652 are part of the lining residues found for the different pathways.



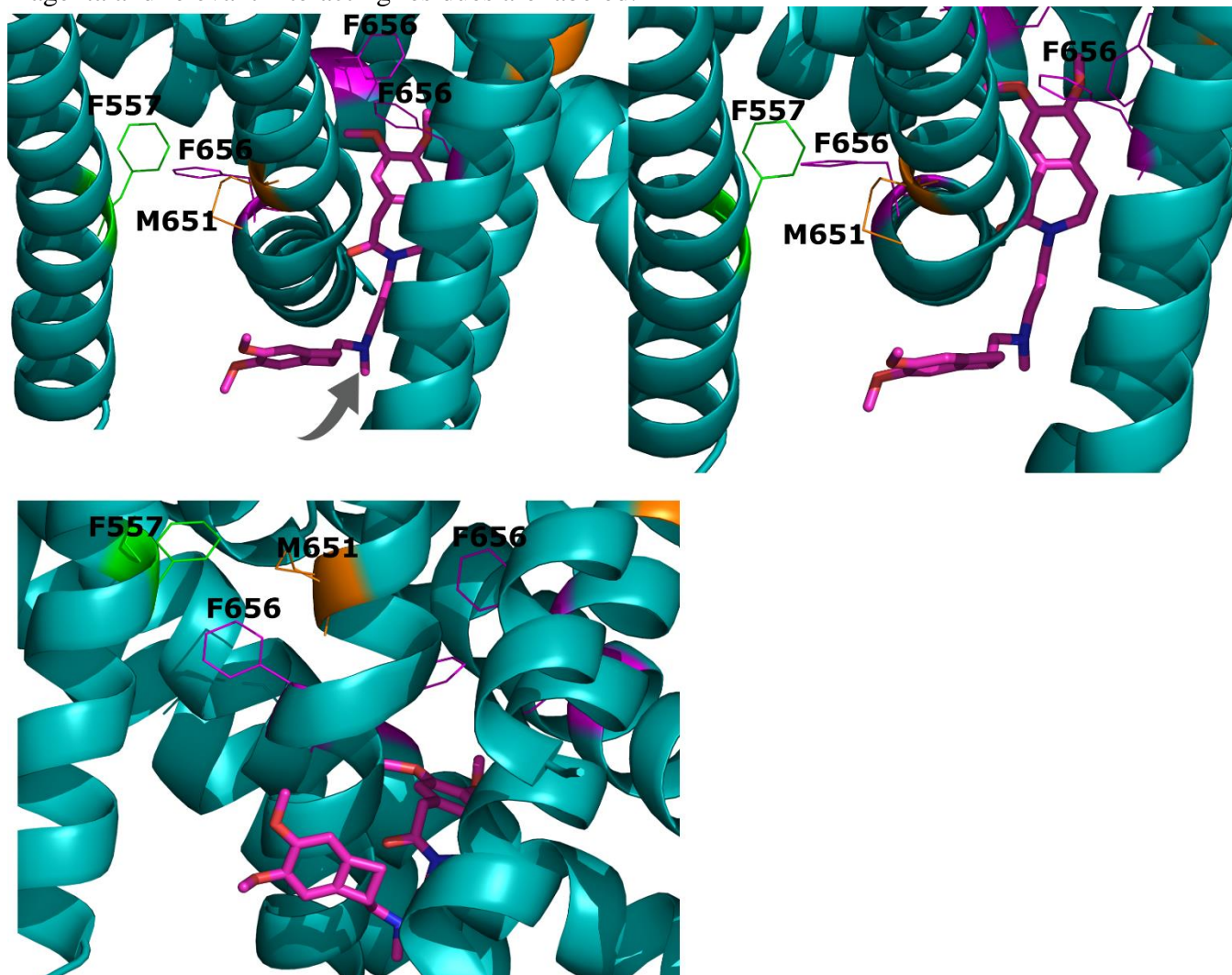
Supplementary Figure 10. Side-view of the ivabradine poses (represented by magenta stick) shown for WT, M651T, M651T/F557L and F557L hERG1 channels. The Pore Domain is depicted in teal, Voltage Sensing Domain is in green.



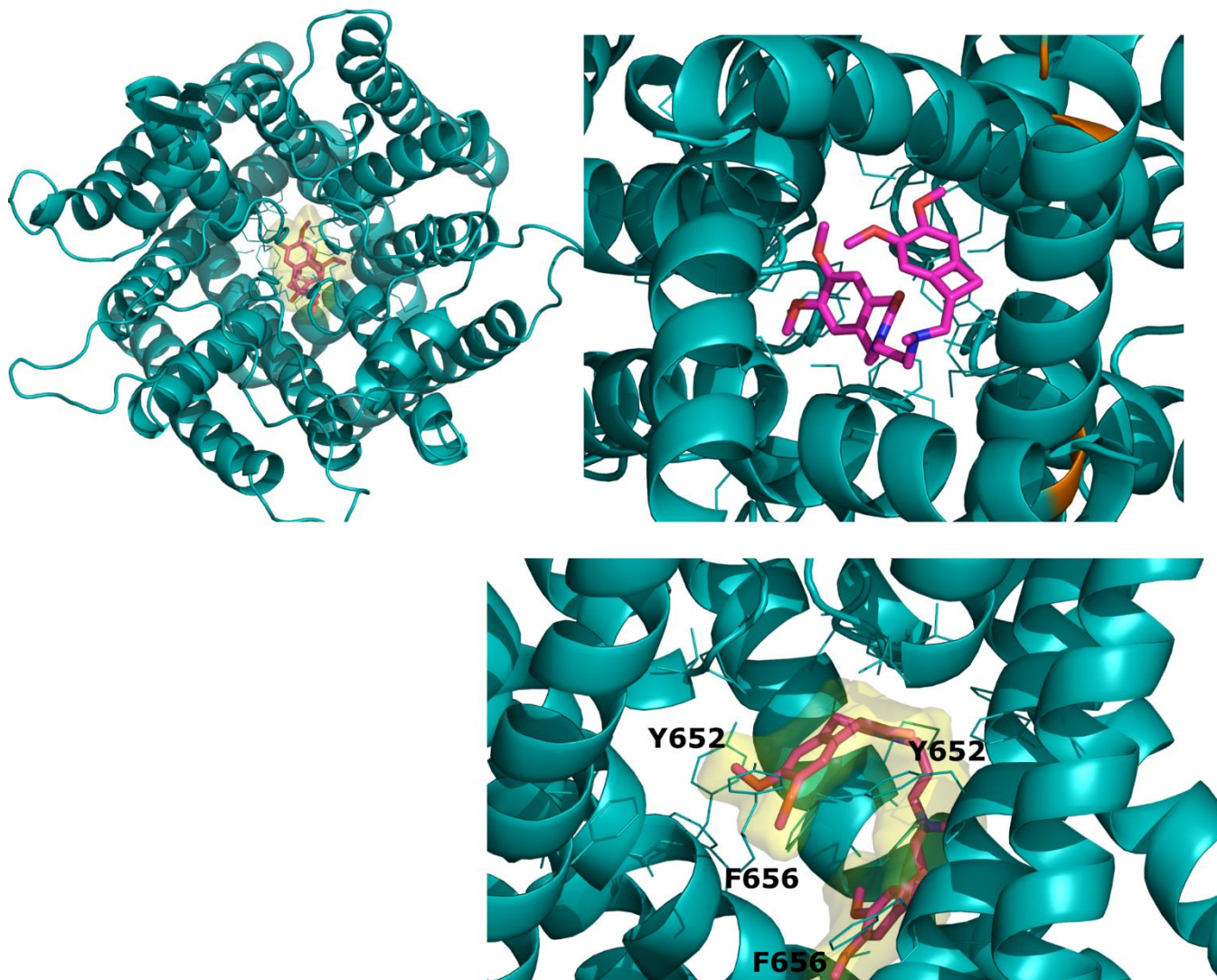
Supplementary Figure 11. Zoom-in topology of the ivabradine binding to different sites of the Pore Domain (PD) and the Trans-Membrane Domain (TMD) of WT and mutant hERG1 (One of the monomer structure is removed for clarity).



Supplementary Figure 12: Topology of the lipid-facing binding pocket. Ivabradine is shown in magenta and relevant interacting residues are labeled.



Supplementary Figure 13: Top- and side-views of the intra-cavitary binding pocket in hERG1. Ivabradine is shown in magenta and relevant interacting residues are labeled.

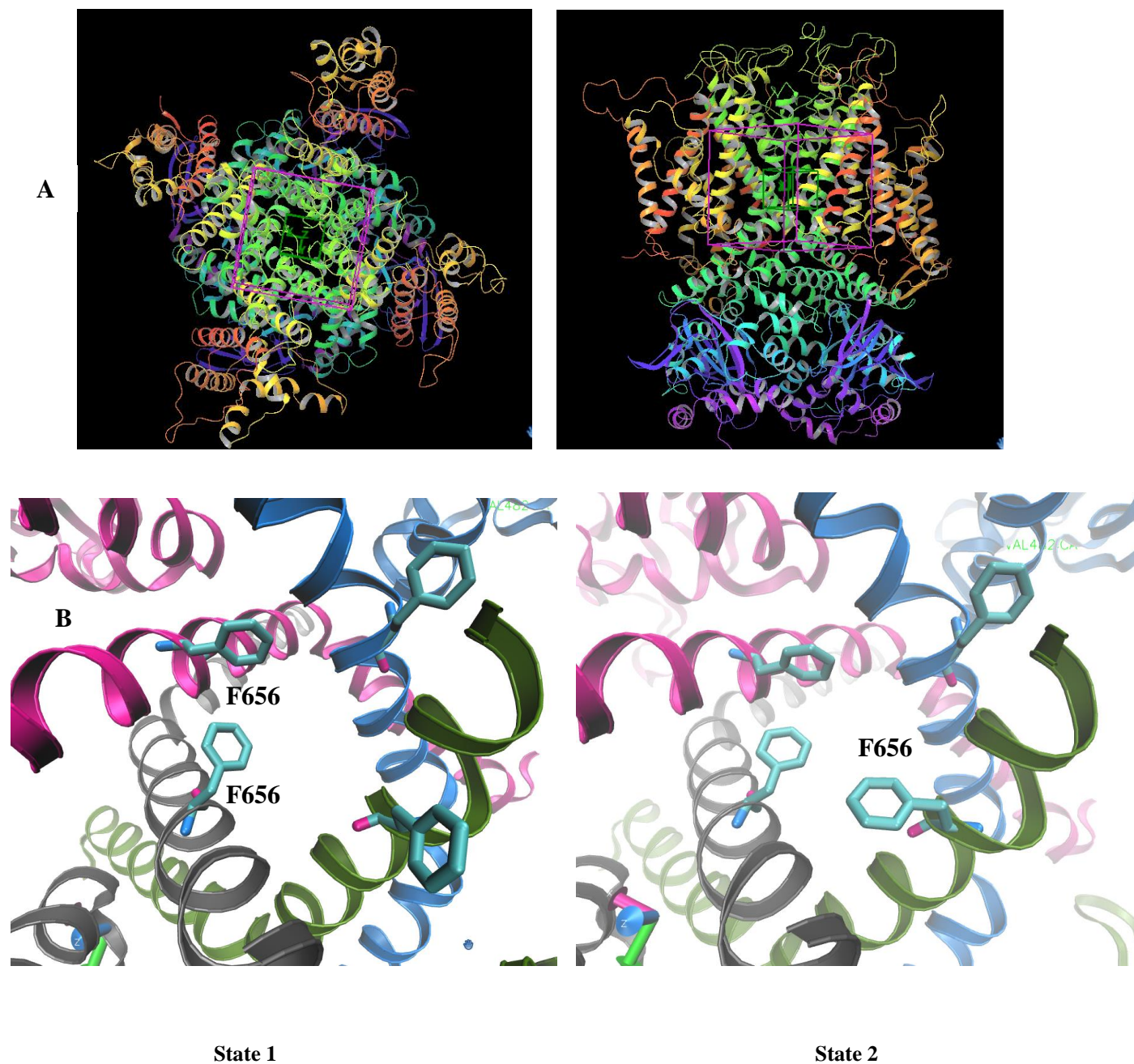


Supplementary Table 4: The energy score results obtained from the X.P. docking of ligands (drugs) in their cationic form to three different states of hERG1 observed in MD simulations. The rendering of the docking volume is shown in the Supplementary Figure 14.

		State1	State2	State 3	Cryo em
	IC50	(kcal/mol)	(kcal/mol)	(kcal/mol)	(kcal/mol)
dofetilide	7.9	-7.6	-10.3	-5.3	-6.0
dronedarone	7.2	-5.7	-4.6	-5.2	-6.6
ebastine	6.9	-7.6	-7.0	-7.0	-6.4
ziprasidone	6.8	-7.9	-5.5	-3.6	-5.5
loratadine	6.8	-8.2	-5.8	-5.3	-4.6
amascrine	6.7	-8.2	-7.1	-5.3	-6.3
mizolastine	6.5	-8.7	-9.3	-9.9	-5.5
carvedilol	6.3	-8.3	-8.5	-5.7	-3.1
ondansetron	6.1	-8.1	-6.8	-6.6	-5.1
chlorpromazine	5.8	-8.8	-6.8	-5.3	-4.5
ketoconazole	5.7	-9.4	-9.2	-5.1	-5.6
ivabradine	5.7	-7.1	-2.7	-4.5	-2.2
quetiapine	5.2	-7.0	-4.0	-5.3	-5.9

State 3 represents the receptor geometry after 1.3 micro-second of all-atom MD simulation. State 1 and State 2 represents two most-populated structural clusters observed in equilibrium MD simulations (k-means clustering with positions of C_α atoms were used to analyze 1.5 micro-seconds of the production simulation).

Supplementary Figure 14 Docking was performed on Maestro (Schrodinger) using 3 different states of the W.T. hERG1. Each ligand was prepared using LigPrep (sampled ring conformations and different state of the charged group corresponding to pH 7.4). Replication of the same dockings with the same receptor structure yielded identical results. **Panel A** shows various views of the docking grid. **Panel B** shows differences in F656 orientation observed in major structural states from all-atom MD simulations.



References

- Appleby IC, Newbury TC and Nichols G (1999) Dofetilide polymorphs, (WO1999021829A1 ed).
- Chothia C (1976) The nature of the accessible and buried surfaces in proteins. *J Mol Biol* **105**(1): 1-12.
- Horvath S (2005) Beta-crystalline form of ivabradine hydrochloride, a process for its preparation and pharmaceutical compositions containing it (US7879842B2 ed), Laboratoires Servier, USA.
- Karimi-Jafari M, Padrela L, Walker GM and Croker DM (2018) Creating Cocrystals: A Review of Pharmaceutical Cocrystal Preparation Routes and Applications. *Cryst Growth Des* **18**(10): 6370-6387.
- Perlovich GL, Kurkov SV, Hansen LKR and Bauer-Brandl A (2004) Thermodynamics of sublimation, crystal lattice energies, and crystal structures of racemates and enantiomers: (+)- and (+/-)-ibuprofen. *J Pharm Sci-US* **93**(3): 654-666.
- Perlovich GL, Volkova TV and Bauer-Brandl A (2006) Towards an understanding of the molecular mechanism of solvation of drug molecules: a thermodynamic approach by crystal lattice energy, sublimation, and solubility exemplified by paracetamol, acetanilide, and phenacetin. *J Pharm Sci* **95**(10): 2158-2169.
- Wimley WC and White SH (1996) Experimentally determined hydrophobicity scale for proteins at membrane interfaces. *Nat Struct Biol* **3**(10): 842-848.
- Zamyatnin AA (1972) Protein volume in solution. *Prog Biophys Mol Biol* **24**: 107-123.